Molecular Biology of the Cell
Vol. 7, 1259–1282, August 1996

Myosin II Transport, Organization, and Phosphorylation: Evidence for Cortical Flow/Solation–Contraction Coupling during Cytokinesis and Cell Locomotion

Robbin L. DeBiasio,* Gregory M. LaRocca, Penny L. Post,† and D. Lansing Taylor

Division of Molecular Sciences, Center for Light Microscope Imaging and Biotechnology, and Department of Biological Sciences, Carnegie Mellon University, Pittsburgh, Pennsylvania 15213

Submitted March 12, 1996; Accepted May 29, 1996
Monitoring Editor: James A. Spudich

The mechanism of cytokinesis has been difficult to define because of the short duration and the temporal–spatial dynamics involved in the formation, activation, force production, and disappearance of the cleavage furrow. We have investigated the structural and chemical dynamics of myosin II in living Swiss 3T3 cells from prometaphase through the separation and migration of daughter cells. The structural and chemical dynamics of myosin II have been defined using the semiautomated, multimode light microscope, together with a fluorescent analogue of myosin II and a fluorescent biosensor of myosin II regulatory light chain (RLC) phosphorylation at serine 19. The correlation of image data from live cells using different modes of light microscopy allowed interpretations not possible from single-mode investigations. Myosin II transported toward the equatorial plane from adjacent regions, forming three-dimensional fibers that spanned the volume of the equator during anaphase and telophase. A global phosphorylation of myosin II at serine 19 of the RLC was initiated at anaphase when cortical myosin II transport started. The phosphorylation of myosin II remained high near the equatorial plane through telophase and into cytokinesis, whereas the phosphorylation of myosin II at serine 19 of the RLC decreased at the poles. The timing and pattern of phosphorylation was the same as the shortening of myosin II-based fibers in the cleavage furrow. Myosin II-based fibers shortened and transported out of the cleavage furrow into the tails of the two daughter cells late in cytokinesis. The patterns of myosin II transport, phosphorylation, and shortening of fibers in the migrating daughter cells were similar to that previously defined for cells migrating in a wound in vitro. The temporal–spatial patterns and dynamics of myosin II transport, phosphorylation at serine 19 of the RLC, and the shortening and disappearance of myosin II-based fibers support the proposal that a combination of the cortical flow hypothesis and the solation–contraction coupling hypothesis explain key aspects of cytokinesis and polarized cell locomotion.

INTRODUCTION

Investigating the mechanism of cytokinesis has been a major target of cell biological research for more than a century (for review, Swann and Mitchison, 1958; Rappaport, 1986; Salmon, 1989; Mabuchi and Itoh, 1992; Satterwhite and Pollard, 1992; Fishkind and Wang, 1995). Today there is good evidence that actin and myosin II play a central role in cytokinesis (Fujiwara and Pollard, 1976; Mabuchi and Okuno, 1977; Kiehart *et al.*, 1982; DeLozanne and Spudich, 1987; Knecht and Loomis, 1987; Schroeder, 1990; Fukui, 1993). Fluores-

* Corresponding author.
† Present address: Department of Biology, Yale University, Kline Biology Tower, Box 208103, New Haven, CT 06520-8103.

© 1996 by The American Society for Cell Biology

cence-based localization methods, applied to fixed cells, have demonstrated the static organization and structure of actin and myosin II in the cleavage furrow (Sanger, 1975; Maupin and Pollard, 1986; Fishkind and Wang, 1993; Mabuchi, 1994). A combination of biochemical, genetic, molecular, biophysical, and structural approaches, applied to a range of organisms, are beginning to reveal important details of the steps, components, and mechanics involved in cytokinesis (Sanders and Field, 1994; Fishkind and Wang, 1995; Miller and Kiehart, 1995). The polar relaxation model (White and Borisy, 1983), an extension of a theory originally proposed by Wolpert (1960), and the equatorial stimulation model (Rappaport, 1971) have served as guides for exploring the global, cellular events responsible for initiating cytokinesis. In addition, three models of force generation at the cleavage furrow have evolved based on the sliding filament theory of actin and myosin II contraction (Fishkind and Wang, 1995). Although progress has been made, the mechanism of cytokinesis continues to elude a detailed definition.

The key to solving the mechanism of cytokinesis is to define the temporal–spatial dynamics of the molecular components (e.g., cytoskeletal proteins), regulatory cascades, cell–cell or cell–substrate interactions, and force production in living cells (Taylor and Wang, 1978, 1980; Taylor *et al.*, 1992). The integration of light microscope imaging technologies and reagents specific for chemical and molecular processes has created an approach for treating living cells as living test tubes for the measurement and manipulation of cell dynamics (DeBiaso *et al.*, 1987; Taylor and Wang, 1989; Wang and Taylor, 1989; Mason, 1993; Giuliano *et al.*, 1995; Giuliano and Taylor, 1995). These tools allow the investigation of dynamic processes globally, while attaining high spatial and temporal resolution. This approach has already yielded important information about the dynamics, during cytokinesis, of actin assembly (Wang and Taylor, 1979), the recruitment of pre-existing actin filaments into the cleavage furrow (Cao and Wang, 1990a), the cortical transport of actin filaments (Cao and Wang, 1990b), the assembly and disassembly of actin and myosin II-based fibers (Mittal *et al.*, 1987; Sanger *et al.*, 1989), the potential relationship between stress fibers and fibers in the cleavage furrow (Sanger *et al.*, 1994), the global contractile activity during cytokinesis (Wang *et al.*, 1994), and the role of myosin II in postmitotic cell spreading (Cramer and Mitchison, 1995). The dynamic changes in free $[Ca^{2+}]$ have been investigated, but the results have been variable (Salmon, 1989; Hepler, 1994), although recent evidence supports a direct role of free $[Ca^{2+}]$ in cytokinesis (Fluck *et al.*, 1991; Ciapa *et al.*, 1994; Chang and Meng, 1995). Burton and Taylor (unpublished data) have recently defined the sites of traction forces applied to the substrate during cytokinesis using an improved "rubber sheet" method. The development of more powerful and specific reagents and imaging technologies, coupled with genetic and molecular-genetic manipulations of cells and molecules, will accelerate the rate and extent of our understanding of the mechanism of cytokinesis.

We have built on the technical developments in reagent chemistry and imaging technology, as well as the biological studies described above, to explore the dynamics of myosin II transport, phosphorylation, contraction, and organization from prophase to migration of the daughter cells. We have used a fluorescent analogue of myosin II to define the dynamic distribution of myosin II (DeBiasio *et al.*, 1988; Giuliano *et al.*, 1990; Kolega and Taylor, 1993), a biosensor of myosin II regulatory light chain (RLC) phosphorylation to map the dynamics of phosphorylation (Post *et al.*, 1994, 1995; Giuliano *et al.*, 1995) and a fluorescent volume marker to quantify the relative concentration of myosin II (DeBiasio *et al.*, 1988). The multimode light microscope has been used to correlate dynamic results using two-dimensional and three-dimensional fluorescence, ratio imaging for local myosin II concentration and phosphorylation, video-enhanced contrast to determine cell cycle stage, and reflection interference contrast for cell–substrate dynamics (Giuliano *et al.*, 1990; Taylor *et al.*, 1992; Farkas *et al.*, 1993). The combined use of the reagents and the multimode light microscope has allowed us to address three major questions concerning cytokinesis: 1) How does the cleavage furrow form? 2) What do the dynamics and the structure of the cleavage furrow tell us about the possible mechanisms of force production? and 3) Is there a relationship between the mechanisms of cytokinesis and polarized cell locomotion?

MATERIALS AND METHODS

Fluorescent Analogues, Biosensors, and Volume Indicators

Smooth muscle myosin II was purified from fresh turkey gizzards (Pound's Turkey Farm, Leechburg, PA), which were stored frozen at −80°C until purification using the procedure described by Sellers *et al.* (1981), with minor modifications as described in DeBiasio *et al.* (1988). Purified myosin II was labeled with tetramethylrhodamine-5 (and -6) iodoacetamide (AR-myosin II) (Molecular Probes, Junction City, OR) (DeBiasio *et al.*, 1988; Hahn *et al.*, 1993). AR-myosin II incorporation and distribution has been well-characterized in nonmuscle cells (DeBiasio *et al.*, 1988; Sanger *et al.*, 1989; Kolega and Taylor, 1993; Verkhovsky and Borisy, 1993; Sanger *et al.*, 1994; Cramer and Mitchison, 1995), including colocalization by immunofluorescence and electron microscopy.

A fluorescent, low molecular weight volume indicator capable of penetrating throughout the cell and into the peripheral regions of the cell was used to normalize the myosin II images for changes in pathlength throughout the cell (see Image Processing and Analysis below). OCy-3 (5, 5′-Disulfo-3, 3′-([ϵ]-carboxypentynyl)-oxacarbocyanine) (Hong *et al.*, 1992) was synthesized by Dr. Ratnakar Mujumdar, and a dextran conjugate (molecular weight 10 kDa), (OCy-3-dex-10K) was prepared by Dr. Kenneth Giuliano (available from

Amersham International, plc as Cy2). OCy-3-dex-10K is pH insensitive and more photostable than fluorescein-labeled dextrans. The enhanced photostability of this volume indicator, compared with fluorescein dextran (DeBiasio *et al.*, 1988), enabled it to be used in time-lapse sequences for ratio image analysis (see Ratio Imaging below). Cascade Blue dextran (molecular weight 10 kDa) (CB-dex-10K) (Molecular Probes) was used as the volume indicator in experiments with the myosin II phosphorylation biosensor.

The biosensor for myosin II phosphorylation of the RLC at serine 19 was prepared as described previously (Post *et al.*, 1995). The biosensor depends on energy transfer from fluorescein-labeled RLCs to rhodamine-labeled essential and/or heavy chains. The change in energy transfer is due primarily to phosphorylation of serine 19 by myosin light chain kinase (MLCK). Protein kinase C induced a 3.4% increase in energy transfer, whereas MLCK induced a 26.0% increase (Post *et al.*, 1995).

OCy-3-dex-10K was coinjected with AR-myosin II, and the biosensor for myosin II phosphorylation was coinjected with the volume indicator CB-dex-10K. Both AR-myosin II and the myosin II phosphorylation biosensor were prepared for microinjection in Injection Buffer (2 mM HEPES, 100 mM NaCl, 0.2 mM MgATP, 0.1 mM EGTA, 1 mM DTT, pH 7.5). The microinjection solution was clarified by centrifugation for 5 min at 76,500 × *g* in a Beckman Airfuge (Beckman Instruments, Palo Alto, CA). The final OCy-3-dex-10K and the CB-dex-10K concentration was 3 mg/ml, and the final AR-myosin II or phosphorylation biosensor concentration was 4 mg/ml in the clarified supernatant for microinjection.

Cell Culture and Microinjection

Swiss 3T3 fibroblast cells (CCL92; American Type Culture Collection, Rockville, MD) were maintained in Dulbecco's modified Eagle's medium (DMEM; Life Technologies, Grand Island, NY), pH 7.4, containing 2 mg/ml penicillin, 0.05 mg/ml streptomycin, and 10% calf serum (complete DMEM [c-DMEM]). Subconfluent 3T3 cells were subcultured every 3 d by trypsinization using 0.05% trypsin and 0.02% EDTA in Ca-Mg-free saline solution (Life Technologies). All cell cultures were incubated in a humidified 5% CO_2 environment at 37°C. Cell passage number ranged from 119 to 125.

To obtain subconfluent, log-phase cells on 40-mm-round glass coverslips (Fisher Scientific, Pittsburgh, PA), 1–2 × 10^4 3T3 cells in c-DMEM were seeded into 60 mm culture dishes (Corning Glass Works, Corning, NY) containing the 40 mm coverslips. Cells were used 3–4 d after plating. Random log-phase 3T3 cells (typically >100 cells/coverslip) were microinjected (Amato *et al.*, 1983) with a mixture of AR-myosin II and the volume indicator OCy-3-dex-10K, or the phosphorylation biosensor and the volume indicator CB-dex-10K, as described above. Medium was changed to phenol red-free c-DMEM that had been equilibrated for a minimum of several hours in a 37°C, 5% CO_2 incubator. Microinjected cells on the coverslips were allowed to recover 30 min in an incubator before mounting in a cell chamber for the microscope (see below). Image acquisition began 1–2 h after mounting the cells, in the cell chamber, on the microscope (see below).

Multimode Light Microscopy

The multimode light microscope is an automated microscope based on the Zeiss Axiovert microscope (Thornwood, NY). Optical and mechanical modifications were made to allow computer control of three camera options, fluorescence filter sets, neutral density filters, x, y, z stage positions, illumination paths, and distinct modes of light microscopy (Giuliano *et al.*, 1990; Taylor *et al.*, 1992; Farkas *et al.*, 1993). We correlated image data using time-lapse two-dimensional fluorescence, three-dimensional fluorescence, ratio imaging, video enhanced contrast-differential interference contrast (VEC-DIC), and reflection interference microscopy (RIM) modes.

Coverslips with the injected cells were rinsed and mounted with equilibrated (5% CO_2, 37°C) phenol red-free c-DMEM and placed in a sealed environmental chamber on a temperature-controlled stage of the Multimode microscope as described previously (Kolega and Taylor, 1993). Optical components included a ×63 Plan-Neofluar objective, 1.25 numerical aperture (Zeiss), fluorescein (485 nm excitation filter with a 22 nm bandpass, 510 nm longpass dichroic, 530 nm emission filter with a 30 nm bandpass), rhodamine (540 nm excitation filter with a 23 nm bandpass, 572 nm longpass dichroic, 590 nm emission filter with a 35 nm bandpass), and Cascade Blue (355 nm excitation filter with a 40 nm bandpass, 400 nm longpass dichroic, 450 nm emission filter with a 50 nm bandpass) filter sets. Fluorescence, RIM, and DIC images were collected using a cooled CCD camera with a 576 × 384 Thompson chip (Photometrics, Tucson, AZ) as 16-bit data. A video camera (C2400 Newvicon, Hamamatsu Photonics, Bridgewater, NJ) was also used for VEC-DIC for focusing and monitoring cells. To minimize exposure to fluorescence excitation, microinjected cells were identified and selected using the rhodamine filter set with a neutral density (ND) filter of 1.5 and a single-stage intensified CCD camera (XC-77/C2400; Hamamatsu Photonics, Bridgewater, NJ). Minimal excitation of fluorescence was achieved by using ND filters and short exposure times to limit photobleaching and phototoxicity. Careful attention to the total dose of excitation to the cells permitted up to 40–50 individual myosin II images to be obtained as two-dimensional time-lapse sequences, three-dimensional stacks, or combinations. All cells examined in this study underwent normal cell division and polarized cell locomotion during and after data acquisition. Temporal and spatial resolutions were trade-offs to the total dose of excitation required (Bright and Taylor, 1986; Bright *et al.*, 1987; Taylor and Salmon, 1989).

Fluorescent cells were logged into the computer-controlled stage list that recorded the x, y, and z coordinates of each stage position. The stage list routine enabled all logged cells to be revisited at selected time intervals throughout the course of the experiment for time-lapse imaging of multiple cells on the same coverslip. Monitoring the stage of the cell cycle and focusing was performed by VEC-DIC, using a 640 longpass filter to avoid excitation of the AR-myosin II, phosphorylation biosensor, and volume indicator. Each stage position was automatically scanned over time and monitored by VEC-DIC to identify cells entering cell division. These cells were selected for three-dimensional analysis and/or further time-lapse investigation with the various modes of light microscopy. RIM images, showing cell-to-substrate contact adhesion, were acquired using the three wavelength method (excitation 530, 570, and 640 nm) (Bereiter-Hahn *et al.*, 1979). Images were sequentially acquired in the following order using the cooled CCD camera: 1) RIM (0.05–0.1 s exposure, ND 0.3–0.6); 2) VEC-DIC (0.1 s exposure, ND 1.3); 3) myosin II analogue or phosphorylation biosensor, (0.5 s exposure, ND 0.6); and 4) volume indicator (0.5 s exposure, ND 0.6).

Three-dimensional myosin II image stacks were acquired at selected time points after acquiring single images at the central focal plane of the other modes of light microscopy (see above). Myosin II stacks were acquired using the cooled CCD camera with an exposure time of 0.3–0.5 s and an ND of 0.3–0.6. Stacks consisted of approximately 30–40 images with a 0.2-μm step size.

All images were acquired using BDS-Image software (now STC-View, a Carnegie Mellon enhancement of the original BDS-Image package). STC-View allows rapid acquisition of both two-dimensional and three-dimensional data. Acquired images were stored in the RAM of a Macintosh Quadra 950 computer (Apple Computer, Cupertino, CA). During acquisition, images in RAM were written out to a 1 Gb external hard disk as CPU time allowed. At the end of the experiment, data were backed up to a 4 Gb DAT storage tape (Microtech International, East Haven, CT) for long-term storage.

Image Processing and Analysis

Images were processed on a Macintosh IIfx or Quadra 950 computer (Apple Computer) using STC-View's three-dimensional and Movie Processing application (MPROC). Time-lapse "movie" sequences of

the individual parameters (VEC-DIC, RIM, myosin II, biosensor, volume, three-dimensional slices), as well as processed ratio sequences, were produced using QuickTime (Apple Computer) to provide a method for rapid display of the temporal changes in each parameter. Unless otherwise stated, the time of the first image in a time-lapse sequence was designated as time 0 (t = 0.00') regardless of the cell division phase, and all successive images in the sequence were reported as the number of minutes elapsed after the first image.

Myosin II Ratio Imaging. Ratio imaging permits interpretation of the local, relative concentration of myosin II by normalizing the images for pathlength and accessible volume with a volume indicator (Tanasugarn *et al.*, 1984; DeBiasio *et al.*, 1988; Kolega and Taylor, 1993; Giuliano and Taylor, 1994). Before ratio image analysis, images of the OCy-3-dex-10K volume indicator for each myosin II sequence were normalized for photobleaching. Photobleaching curves were generated from time-lapse images of cells loaded with OCy-3-dex-10K using the same imaging conditions as the experiment. Because the volume indicator does not bind to intracellular components, change intensity because of interactions within the cell, or leak out of the cell (DeBiasio *et al.*, 1988; Kolega and Taylor, 1993), the total fluorescence of the cell remains relatively constant as the cell changes shape during cell locomotion or division. Thus, a decrease in total fluorescence of the volume images during an image acquisition series is due to photobleaching. A correction factor for each time point was generated to correct the degree of photobleaching. Under the illumination conditions described above, a sequence of volume indicator images using OCy-3-dex-10K showed ~14% photobleaching after a 30-image sequence. AR-myosin II photobleached 6% after a 30-image sequence. Because the photobleaching of AR-myosin II was minimal and total cell myosin II fluorescence was not uniformly distributed like the volume indicator, the AR-myosin II images were not corrected for photobleaching.

Time-lapse ratio image analysis for myosin II concentration was performed using an interactive computer ratio processing program in STC-View's MPROC. Each sequence of myosin II images was background-subtracted using an internal region of interest (ROI) on each image in the sequence. The matching sequence of volume images was also background-subtracted using an internal ROI, and then normalized for photobleaching as described above. The volume images were also smoothed using a 3 × 3 kernel (Bright *et al.*, 1987), and the sequence was registered to its corresponding myosin II sequence. The cell or cells of interest in the sequence were masked using an interactive draw routine to exclude other nondividing fluorescent cells or noncellular fluorescence from ratio computation. The series of masks were applied to the registered myosin II and volume image sequences, and ratio image sequences were generated by dividing the myosin II images by the corresponding volume indicator images. The resulting series of ratio images were maintained as 16-bit images, and statistics including the min, max, mean, sum, number of pixels, variance, and SD were stored in Excel (Microsoft, Redmond, WA) data files. The entire sequence was internally scaled, and pseudocolor maps were automatically applied to the sequence to obtain pseudocolor time-lapse movies. Pseudocolor wedges indicating the corresponding color and ratio values also were generated. Selected individual ratio images within a sequence were used for figure preparation.

Ratio Imaging of Biosensor. Photobleaching during the double excitation required for energy transfer was minimized by collecting the fluorescein emission via direct excitation of the fluorescein dye and rhodamine emission via direct excitation of the rhodamine dye. Changes in energy transfer were detected by dividing the phosphorylation-insensitive rhodamine emission image by the fluorescein (phosphorylation-sensitive, or donor quenched) emission image to produce a ratio image. This ratio is an indicator of energy transfer and is referred to as the " phosphorylation ratio," although it is not a true "energy transfer ratio." Because both the donor and acceptor dyes are on the same protein, the rhodamine image normalizes the fluorescein image to differences in cell pathlength, accessible cell volume, and local protein concentration, whereas the fluorescein image shows phosphorylation-dependent quenching of the donor.

The rhodamine myosin II, fluorescein myosin II RLC, and CB-dex-10K volume images were background-subtracted, registered, and masked (see Myosin II Ratio Imaging above) before the division of the rhodamine myosin II image by the fluorescein myosin II image (myosin II phosphorylation ratio image), or the division of the rhodamine myosin II image by the CB-dex-10K volume image (myosin II ratio image). Two separate ratios were generated from these three images: rhodamine myosin II/CB-dex-10K mapped the relative concentration of myosin II, whereas rhodamine myosin II/fluorescein myosin II RLC mapped the relative phosphorylation of myosin II. Only one set of rhodamine, fluorescein, and CB-dex-10K volume images was acquired for each of the 43 cells used for the detection of spatial changes in myosin II phosphorylation patterns during division. This study compared regions of maximal myosin II phosphorylation with regions of elevated myosin II concentration. The myosin II phosphorylation ratios and the myosin II ratios were scaled independently (Figure 9) for enhanced visualization of the maximal and minimal regions of relative myosin II phosphorylation and concentration. Therefore, no interpretations between the maximal ratio values of the myosin II concentration and phosphorylation level, or between individual cells, can be made from this portion of the study. The ratios were pseudocolored to enhance the visualization of patterns. High ratio values were represented in red, lower ratio values in blue.

To detect changing patterns of myosin II phosphorylation in the same dividing cells over time, 15 cells were studied at two or three different stages of cell division. Test images indicated that the fluorescein myosin II RLC image of the biosensor bleached at a mean rate of 13.3% during the acquisition of the second image and an additional 5.8% during the third image. The 2- or 3-image sequences were corrected for photobleaching of fluorescein before generating the myosin II phosphorylation ratios (Figure 10). These ratio sequences were internally scaled, and the highest ratio value in the series was pseudocolored red and the lowest ratio value was pseudocolored blue. Therefore, changes in the spatial distribution of myosin II phosphorylation were detected over time. For comparison, the ratio values were reported as a fold-response, where the lowest ratio value (blue) was given a value of 1.0 and the highest ratio value (red) was given as a factor (e.g., 2.5×) to represent the range of the response. No quantitative levels of myosin II phosphorylation are provided by the analysis of these time-lapse ratio sequences, but the data demonstrate spatial patterns of myosin II phosphorylation during cell division.

Myosin II Image Enhancement. Time-lapse sequences of myosin II fluorescent analogue images were processed for display purposes of fiber detection by background subtraction of an internal ROI on each image and sharpening using a factor of 0.3 (factor range 0.00–1.00). The same enhancement protocol was also applied to the volume indicator as a control. Myosin II image sharpening procedures were not used during ratio image analysis.

VEC-DIC Image Enhancement. DIC images were processed for image enhancement (VEC-DIC) by mottle division of a defocused background image and sharpening using a factor of 0.10 (factor range 0.00–1.00).

RIM Image Processing. For figure display, RIM images were enhanced by mottle division of a focused background image and sharpening using a factor of 0.10 (factor range 0.00–1.00).

Line Profile Analysis. Line profile analysis yielded fluorescence intensity and ratio value profiles along selected lines through the cell on myosin II, volume, and ratio images. A line profile analysis program in STC-View was used to acquire the data along the line drawn through the cell. The data files were transferred to KaleidaGraph (Synergy Software PCS, Reading, PA) for graphic representation.

Fiber Length Measurements. The lengths of fibers containing myosin II, measured in micrometers, were obtained using an interactive line drawing program in STC-View. The criteria for determin-

ing the ends of fibers for the measurement of fiber length were a decrease of >70% fluorescence intensity along a visible myosin II fiber and/or a drop in intensity, measured over a distance greater than the sarcomeric variation along the fiber that was similar to the diffuse, nonstructured intensity of the region surrounding the fiber. Lines were drawn along selected fibers, and the lengths of the lines were stored as numbers of pixels. The total length of each fiber in micrometers was calculated by multiplying the number of pixels by the factor relating the pixel size to micrometers (Bright and Taylor, 1986).

Calculation of Rate of Fiber Transport and Shortening. The rate of fiber transport or fiber shortening was obtained by using a line measurement program in STC-View. Time-lapse sequences of myosin II images were registered before distance measurements were calculated.

For rates of fiber transport, a series of lines were drawn from a fixed point outside the cell to the same myosin II fiber on successive images. The distance of fiber translocation, given in pixels, was multiplied by the factor relating the size of the pixel, in micrometers. The difference in the distance that the myosin II fiber traveled over the time interval between measurements yielded a rate of movement measured in micrometers/min. The data were transferred to KaleidaGraph (Synergy Software PCS), where the distance was plotted against the time intervals to examine the linearity of the rate of fiber movement. Statistics from cell studies yielded a mean rate of movement, along with the min, max, SE, SD, and variance.

For fiber-shortening rates, the length of the same fiber (see Fiber Length Measurements above), was calculated on successive, registered myosin II images. The fiber length in micrometers was plotted against time in KaleidaGraph (Synergy Software PCS) to obtain a rate of fiber shortening in micrometers/min and to examine the linearity of the rate over time. Statistics yielded a mean rate of fiber shortening, along with the min, max, SE, SD, and variance.

Three-Dimensional Image Analysis. Three-dimensional myosin II stacks were deconvolved in the three-dimensional application in STC-View, using the nearest-neighbor deconvolution routine and an MC3200NU coprocessor board (Mercury Computer Systems, Lowell, MA) installed in the work station. Nearest-neighbor deconvolution removed out-of-focus fluorescence from each optical section of the three-dimensional stack (Agard, 1984). After deconvolution, the images in the three-dimensional stacks were enhanced for single-image display by applying a fixed scaling factor to all images in the stack and sharpening each image in the stack by using a factor of 0.15 (factor range 0.00–1.00). The three-dimensional structure obtained by the nearest-neighbor algorithm was qualitatively the same as that obtained using a laser scanning confocal microscope (Zeiss) study of cells injected with the myosin II analogue, fixed, and imaged (our unpublished results). The computational approach was used in these live cell studies, because the dose of excitation required was much less than that required for the laser scanning confocal microscope.

Figure Preparation. Images were grouped using the collage feature in the STC-View software, saved as PICT files, and resized electronically in Adobe 2.5 (Adobe Systems, Mountain View, CA). Images were photographed with a Slidewriter (Model 60–53-0001) and Conductor 2.61 Utility software (AGFA Matrix Division, AGFA, Orangeburg, NY) using Kodak T-Max 100 film or Etkachrome 100 film (Eastman Kodak, Rochester, NY).

RESULTS

Multimode Light Microscopy Permits Cross-Correlation of Distinct Structural and Molecular Dynamics in Living Cells

Multiple modes of light microscopy, acquired over time from prophase to the separation of daughter cells, permitted the correlation of structural and molecular events during cell division (Figure 1). The computer-controlled Multimode microscope, using an automated, rapid acquisition program, acquired up to five parameters at each stage position over time. Cycling 3T3 fibroblasts were followed through cell division and VEC-DIC, RIM, myosin II fluorescent analogue, myosin II phosphorylation biosensor, volume indicator, and three-dimensional image stacks were acquired. Ratio images were generated for each time point after data acquisition for relative myosin II concentrations and phosphorylation measurements. Ratio imaging is a critical tool for quantifying fluorescence measurements, because quantitative interpretation of single-fluorescence, two-dimensional images is not possible (Tanasugarn *et al.*, 1984). Time-lapse image "movies," created for each parameter, permitted the correlation of changes in cell–substrate adhesion, the dynamic distribution of myosin II, regions of elevated myosin II concentration relative to a volume indicator, phosphorylation of the RLC of myosin II at serine 19, and the three-dimensional organization of myosin II during cell division. The organization of myosin II, defined by three-dimensional optical sections, also enhanced interpretations of data obtained from ratio images and two-dimensional myosin II fluorescent analogue, time-lapse sequences. Changes in attachment to the substrate over time provided information on the relationship between possible sites of application of traction forces and the activity of myosin II during cell division. Although multimode microscopy was applied to data acquisition, all modes acquired are not presented in each of the figures in this paper in an effort to conserve space, but important correlations are described in the text. Data were collected on dividing cells that remained relatively flat, as well as on cells that rounded up during division. The basic results were comparable for both phenotypes of dividing cells. Figure 1 depicts multimode image data from one time point from a complete time-lapse sequence during cytokinesis of a rounded cell.

The forming daughter cells shown in Figure 1 were in a complex configuration, with one daughter cell attached to the substrate more closely than the other (Figure 1, A and B, arrow). Information on the relative concentration of myosin II obtained from the ratio image (Figure 1E) was supported by the three-dimensional optical sections (Figure 1, F–T). Three-dimensional optical sections confirmed the higher concentration of myosin II in the cortex and demonstrated punctate myosin II, including myosin II in fibers, throughout the cell, with an elevated concentration of myosin II in the cleavage furrow. Fibers containing myosin II were observed in the interzone (region between the separating chromosomes or re-forming nuclei) (Figure 1D) in all cells studied, but three-dimen-

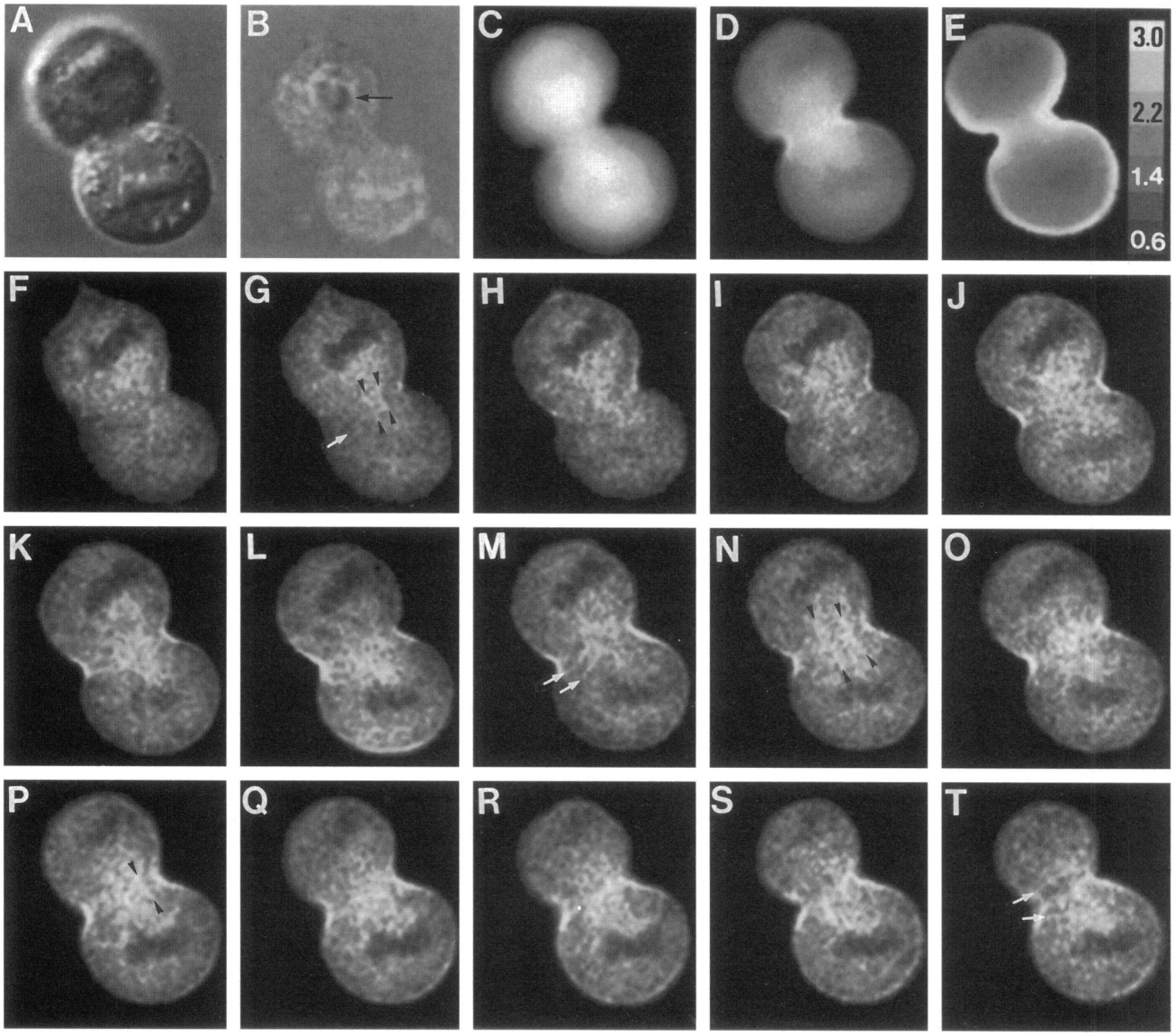

Figure 1. Multimode light microscope analysis of the distribution of myosin II in a live fibroblast during cytokinesis. Fibroblasts were microinjected with a mixture of AR-myosin II and the volume indicator OCy3-dex-10K, and a rapid-acquisition sequence of two-dimensional and three-dimensional images was collected in the order shown. The VEC-DIC image (A) indicated that this live cell was undergoing cytokinesis and had rounded significantly during the process of cell division. The RIM image (B) revealed that during cytokinesis the cell had lost all focal contact with the substrate but remained attached to the substrate by a central close contact located under one daughter cell (B, arrow). The volume image (C) and the myosin II image (D) were used to generate the myosin II ratio image (E). The relative myosin II concentration was normalized for accessible volume and path length by dividing the myosin II image by the volume image, with the higher gray values in the cortex and the interzone corresponding to a higher relative concentration of myosin II in these regions. Pseudocolor mapping of ratios was used in other figures to optimize the presentation of spatial patterns of ratio values. Sequential three-dimensional optical sections were acquired with 0.2-μm z-spacing, starting near the bottom of the cell (F) through the upper region of the top daughter cell and the central region of the bottom daughter cell (T). The distance between the images (F–T) is 0.6 μm, because every third image in the stack is displayed. Punctate myosin II, as well as a complex network of short fibers containing myosin II, was located throughout the volume of the cell. Fibers containing myosin II were detected in the interzone. Fibers in the interzone were observed parallel (e.g., G, M, and T, white arrows), perpendicular (e.g., G, N, and P, black arrowheads), and at various angles to the equator. The distribution of myosin II in the optical sections correlated with regions of elevated myosin II concentration detected in the ratio image (E). Bar, 6.5 μm.

sional optical sections indicated that these fibers were located throughout the volume of the interzone (Figure 1, F–T). Therefore, myosin II is not simply organized as a "purse string" in the cleavage furrow, but exhibits a complex three-dimensional organization (see below).

Four Discrete Components of Directed Myosin II Transport Are Detected from Anaphase to the Separation of Daughter Cells

1) Myosin II Punctate Structures and Fibers Transport into the Equatorial Plane during Anaphase and Telophase. During prometaphase to telophase, myosin II was detected throughout the cell (Figure 2, A–E) in a punctate distribution that was clearly less diffuse than the volume marker image taken at the same plane of focus and processed in the same way (Figure 2F). Myosin II was detected primarily as spots and short punctate "fibers" containing myosin II that ranged in size from <1 μm to ~3 μm. These spots and punctate fibers were randomly oriented throughout the cell in prometaphase (Figure 2A) through early anaphase (Figure 2B). Myosin II appeared to be present in a more structured form rather than in a diffuse unstructured (disassembled) form (Kitanishi-Yumura and Fukui, 1989; Maupin *et al.*, 1994). These punctate spots and small "fibers" may be related to the network of short myosin II filament bundles (0.33 μm in length) observed in both fluorescence microscopy and electron microscopy in 3T3 fibroblasts by Verkhovsky and Borisy (1993). During late anaphase, more myosin II fibers were observed in the interzone (Figure 2C). The number and length of these fibers increased over time from late anaphase through telophase (Figure 2, C–E).

Two-dimensional time-lapse tracking of individual myosin II "fibers," especially in cells that remained flat, exhibited a directional transport of myosin II toward the equator during anaphase and telophase. Individual "fibers" were tracked, and the distance and direction of movement were measured during defined time intervals. The spread cells selected for two-dimensional time-lapse were 50–80 μm long, measured along the longitudinal axis perpendicular to the equator. Myosin II transport was more difficult to detect in time-lapse sequences of 3T3 fibroblasts that had maximally detached from the substrate and rounded during anaphase and telophase (see Figure 1). Time-lapse analyses demonstrated that "fibers" containing myosin II transported toward the equator from regions adjacent to the separating chromosomes and re-forming nuclei (Figure 3, A–C, black arrows; D, region A). Myosin II spots and punctate "fibers" containing myosin II at the distal regions of the cell during anaphase and telophase moved in all directions, including outward toward the cell periphery (Figure 3, A–C, black arrowheads; D, region B). This transport of myosin II is consistent with the study of Wang *et al.* (1994), which reported the transport of fluorescent beads on the surface of normal rat kidney cells from the more central region of the cell toward the equator during anaphase and telophase, whereas beads at the distal regions of the cells moved in random directions.

Fibers containing myosin II transported toward the equator at a relatively uniform rate of 0.96 μm/min (see Table 1 for statistics). Most fibers were tracked for 3 min (~3 μm) before losing the continuity of their movement. Labeled actin filaments, injected into live normal rat kidney cells, incorporated into the dorsal

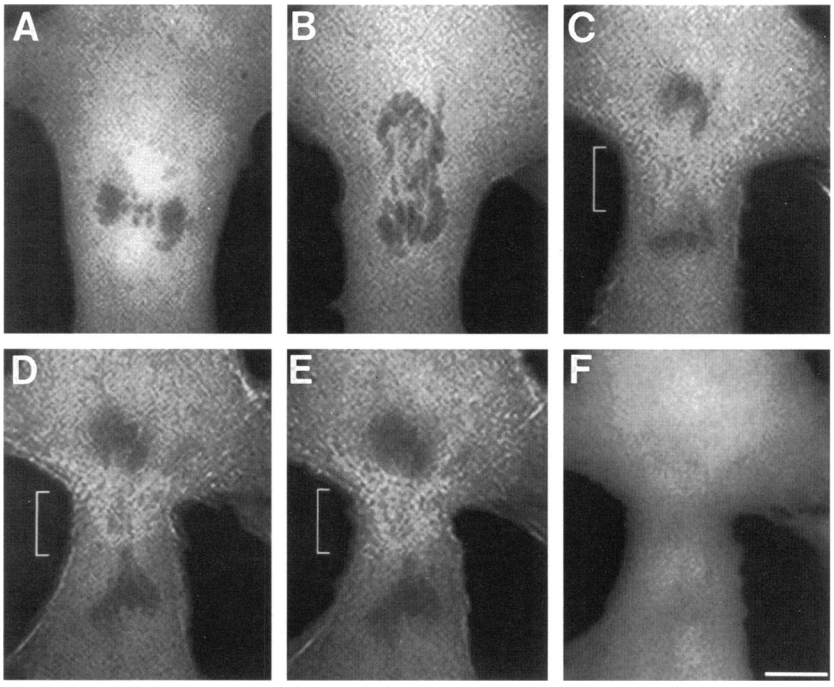

Figure 2. Myosin II organization in the interzone during anaphase and telophase. Punctate spots and short fibers containing myosin II were detected throughout the cell during prometaphase (A) to early anaphase (B). During late anaphase (C), more myosin II punctate spots were detected in the interzone (region between separating chromosomes denoted by the white bracket) and in regions adjacent to the interzone. Well-defined myosin II fibers were detected in the interzone during telophase (D and E). Volume images taken at the same time intervals were also sharpened as a control, and exhibited no structure (F). Time intervals, with the reference point starting at prometaphase, were A, t = 0.0′; B, t = 8.00′; C, t = 10.00′; D, t = 12.00′; E, t = 12.75′; F, t = 12.77′. Bar, 10 μm.

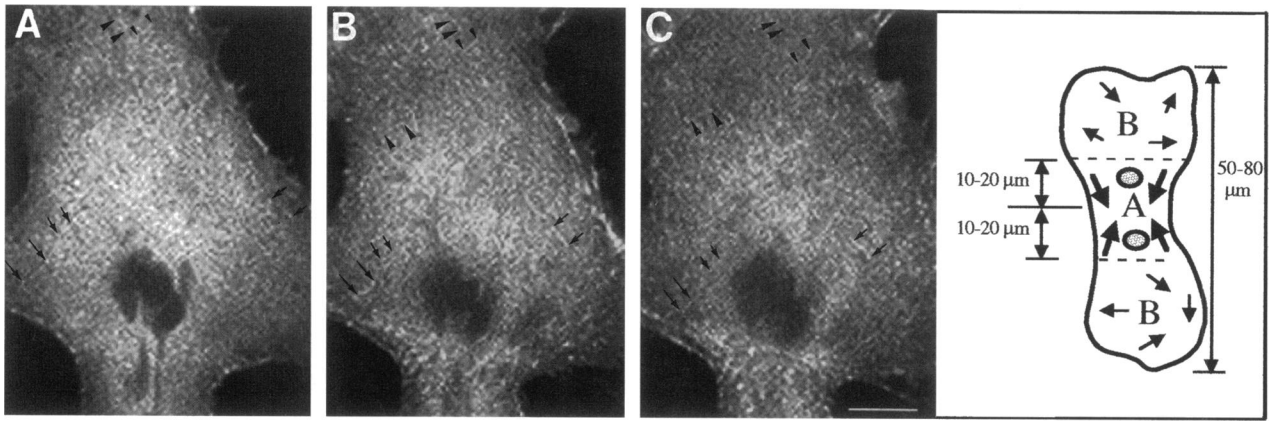

Figure 3. Transport of fibers containing myosin II toward the equatorial plane during anaphase and telophase. Myosin II images were acquired at close time intervals in 3T3 fibroblasts that remained relatively well-spread along the substrate during cell division. Individual short fibers containing myosin II were tracked over time, and the rate and direction of movement were recorded. This myosin II time-lapse sequence shows one forming daughter cell in late anaphase (A) progressing through late telophase (B and C). The time intervals between images were A, t = 0.0′; B, t = 1.5′; C, t = 3.0′. Black arrows to the right and left of the chromosomes in A point to the ends of four of the fibers containing myosin II that were tracked toward the equatorial plane over time in B and C. Black arrowheads in A point to the ends of three of the fibers in the distal regions of the forming daughter cell that moved in various directions over time in B and C. Arrows and arrowheads indicate the direction of fiber transport. A schematic diagram of transport patterns detected during anaphase and telophase is represented in D. In cells that remained spread during division, fibers located within ~10-20 μm of the equatorial plane (region A, shown in panel D) moved toward the equatorial plane, whereas fibers located further away (regions B, shown in panel D) moved in various directions. The mean rate of fiber transport toward the equatorial plane was 0.96 μm/min. Bar, 8 μm.

cell cortex and exhibited a similar transport rate (1.0 μm/min) from the central cell region toward the equator during anaphase and telophase (Cao and Wang, 1990b). It is also evident that actin and myosin II transport together, probably as fibers (Sanger *et al.*, 1994). The transport of fibers containing myosin II into the cleavage furrow is probably one of the mechanisms for forming the furrow.

Table 1. Summary of rates

	Mean (μm/min)	± SD
Myosin II minifilament transport toward furrow during anaphase and telophase	0.96	0.11
Myosin II fiber transport away from equatorial plane during cytokinesis	0.32	0.07
Myosin II fiber shortening in fibers that move away from the equatorial plane during cytokinesis	0.46	0.20
Myosin II fiber shortening near the equatorial plane during cytokinesis prior to midbody formation	0.75	0.15
Cleavage furrow constriction during telophase and cytokinesis	0.61	0.15
Outward movement of myosin II fibers at the periphery during spreading in cytokinesis	0.49	0.16
Outward movement of spreading cell periphery during cytokinesis	0.2–5.0 (range)	
Myosin II centripetal fiber transport from leading edge of separated daughter cells toward 'tail'	0.16	0.07
Myosin II centripetal fiber transport in cycling cells adjacent to dividing cells	0.17	0.02

Measurements were obtained from an average of six cells that remained relatively spread during division. Individual fibers (6–12) were measured within each cell.

In cells that remained spread along the substrate, the period from anaphase onset through telophase was ~5 min. Myosin II fibers moving at a mean rate of 0.96 μm/min could transport ~5 μm in the 5 min period of anaphase and telophase. Fibers in or near the interzone (Figure 3D, region A) would enrich the region near the equator, the interzone, and regions adjacent to the interzone during anaphase and telophase. The transport toward the equator was detected during anaphase and telophase, but directional recruitment was not readily observed during the transition between late telophase and early cytokinesis.

2) Myosin II Fibers Transport Away from the Equator into the Tails of the Two Forming Daughter Cells during Cytokinesis. Fibers containing myosin II, detected within an approximate 3-μm region on each side of the equator during cytokinesis, were usually short and oriented at varying angles in the furrow (Figure 4A). During cytokinesis, myosin II fibers in the interzone and in regions adjacent to the interzone transported away from the equator toward the reforming nuclei (Figure 4, A–D) at a mean rate of 0.32 μm/min (see Table 1 for statistics). The fibers often disappeared as they reached the base of the nuclei

(Figure 4D). A similar phenomenon of fiber loss in the perinuclear region has been observed in serum-deprived and polarized migrating 3T3 fibroblasts (Giuliano and Taylor, 1990; Kolega and Taylor, 1993). Thus, the transport of myosin II out of the cleavage furrow is part of the mechanism for the loss of the furrow structure at the end of the cleavage event. The lower rate of transport out of the furrow compared with the transport into the furrow may indicate that a distinct mechanism is functioning. The role of contraction of these fibers is discussed below.

3) Myosin II Fibers Transport Out into the Spreading, Leading Edges of the Two Forming Daughter Cells during Cytokinesis. Myosin II fibers, near the distal edges of the forming daughter cells, often transported outward during cytokinesis in regions of cell spreading (Figure 5, black arrowheads). These fibers transported outward at a mean rate of 0.49 μm/min (see Table 1 for statistics), whereas other myosin II fibers transported away from the furrow and disappeared near the nuclei (Figure 4). Peripheral cell edges spread outward along the substrate at variable rates ranging from 0.2 to 5.0 μm/min. In some cells, myosin II fibers near the cell periphery (oriented perpendicular to the peripheral cell edge) elongated in regions of cell spreading (Figure 5, A and B, white arrows). Cramer and Mitchison (1995) observed actin fibers in the distal regions moving outward toward the cell periphery in PtK2 cells during cytokinesis. Thus, myosin II and actin appear to play a role in the spreading of the two daughter cells away from the cleavage furrow.

4) Myosin II Fibers Transport Rearward from the Leading Edge after Spreading Stops and Locomotion Begins during Late Cytokinesis and Cell Separation. Fibers containing myosin II exhibited the same pattern of formation and rearward transport from the leading edge to the perinuclear region in the two forming daughter cells as that shown by transverse fibers in polarized, migrating cells (Kolega and Taylor, 1993). Figure 6 shows five time points in a time-lapse series that includes the last stages of cell separation (Figure 6, A–C) and locomotion of separate daughter cells (Figure 6, D and E). Transverse fibers in newly formed daughter cells transport rearward toward the nucleus at a mean rate of 0.16 μm/min (see Table 1 for statistics), similar to the rate determined for the centripetal movement of transverse fibers in cells migrating from a wound (0.2 μm/min) (Kolega and Taylor, 1993). Ratio images demonstrate that there is a gradient of myosin II concentration along the longitudinal axis of the migrating cell, higher at the front of the extending lamellum and lower in the perinuclear region (Figure 6F). The contracting tail also exhibits a higher concentration of myosin II (Figure 6F) (Conrad *et al.*, 1993; Kolega and Taylor, 1993; Post *et al.*, 1995). Therefore, there is a transition from a nonmotile, cleaving stage of cytokinesis to a spreading stage and finally to a locomoting stage of the daughter cells at late cytokinesis. The later stages of cytokinesis share the fiber transport characteristics of freely locomoting cells (Kolega and Taylor, 1993; Giuliano and Taylor, 1994).

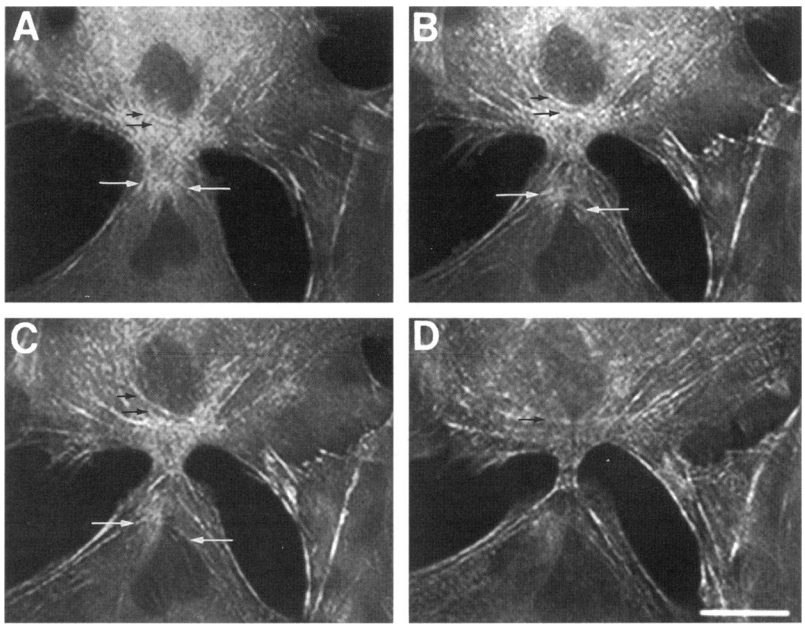

Figure 4. Myosin II fibers transport away from the equator into the tails of the two forming daughter cells during cytokinesis. Time-lapse sequences of myosin II images detected the transport of individual fibers away from the equatorial plane. The fibers disappeared in the perinuclear region. Two myosin II fibers in the upper-forming daughter cell (A, black arrows) moved toward the nucleus over time in B–D. The fiber closest to the nucleus disappeared in the perinuclear region in D. Two fibers in the lower-forming daughter cell (A, white arrows) showed a similar transport toward the nucleus (B and C), and both fibers disappeared in the perinuclear region (D). The time interval between displayed images was A, t = 0′; B, t = 7′; C, t = 10′; D, t = 23′. The mean rate of myosin II fiber transport was 0.32 μm/min. Bar, 13 μm.

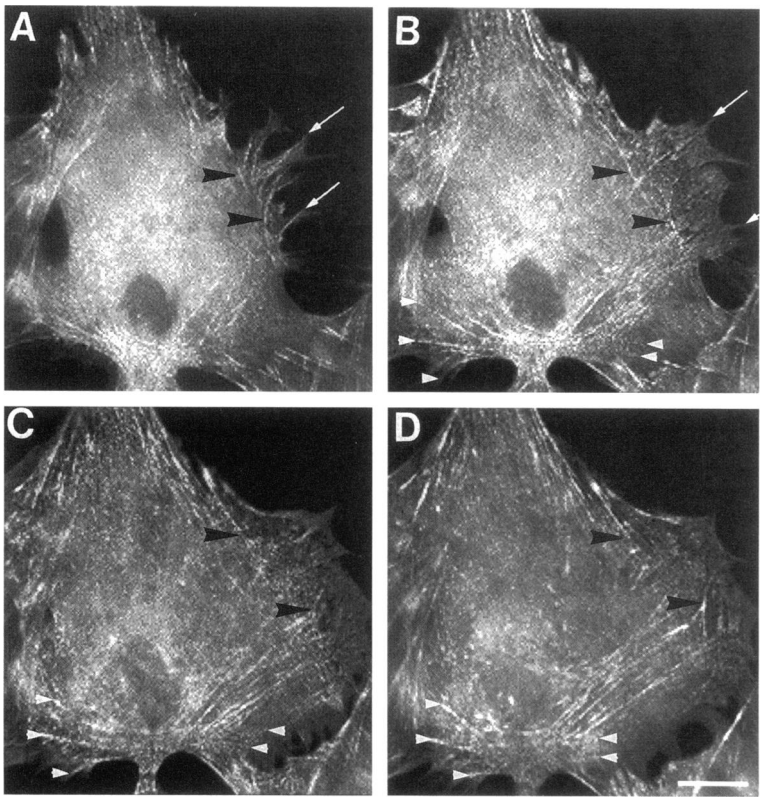

Figure 5. Fibers containing myosin II transport outward into spreading cell edges, and fibers shorten in the tails of forming daughter cells during cytokinesis. Individual myosin II fibers were tracked over time in time-lapse sequences of myosin II images. During furrow narrowing and the transport of myosin II fibers away from the equatorial plane, myosin II fibers also formed in the peripheral regions of the cell. Fibers containing myosin II, oriented perpendicular to the distal cell edges, often elongated outward during cell spreading (A and B, white arrows). During the same period, fibers oriented parallel to the distal cell edges often transported outward (A–D, black arrowheads) at a mean rate of 0.56 μm/min, as the cell edges spread outward or after spreading (rate of spreading ranged from 0.2 to 5.0 μm/min). Fibers in the tails of forming daughter cells shorten over time (B–D, white arrowheads), resulting in a narrowing of the tail region. The number of fibers in the region between the cleavage furrow and nucleus decreased during late cytokinesis as the midbody formed (B vs. D). The time intervals between displayed images were A, t = 0′; B, t = 9′; C, t = 21′; D, t = 32′. Bar, 6.5 μm.

Three Sites of Fiber Shortening Are Identified from Anaphase to Cell Separation

1) The Mean Length of Myosin II Fibers Increased near the Equator during Late Anaphase, Telophase, and Early Cytokinesis and then Decreased over Time during Cytokinesis. The changes in the length of fibers near the equator were calculated from time-lapse sequences of cells that remained relatively flat during division. Fibers within an approximate 3-μm region on each side of the equator were measured during anaphase through cytokinesis, and the mean length of 30 fibers at each selected interval was plotted over time (Figure 7A). The mean length of fibers containing myosin II in the cell represented in Figure 7 increased during late anaphase and telophase (1.5 μm vs. 2.0 μm). The furrow width decreased minimally during the same period the fibers were increasing in mean length. During early cytokinesis, the mean length of fibers increased (2.2–2.5 μm) and then decreased steadily over time during cytokinesis. The width of the cleavage furrow narrowed at a relatively uniform rate during this same period (Figure 7A). As the midbody formed, the furrow width remained relatively constant, fewer fibers were detected in the midbody (see below), and the mean length of fibers remained ~1 μm. The shortening of fibers in and near the furrow during cytokinesis can also be seen in Figures 5 and 6 (arrowheads). Fiber shortening has been measured in Swiss 3T3 cells using both direct measurement and photobleach marking methods (Kolega *et al.*, 1991).

The lengths of individual fibers containing myosin II were measured within an approximate 6-μm region at the equator in successive time-lapse images during cytokinesis. Fibers near the equator shortened at a relatively linear mean rate of 0.75 μm/min (Figure 7, B–J; see Table 1 for statistics). The shortening of fibers near the equator was detected during the early period of furrow narrowing and continued through late cytokinesis. The furrow width in the same cell depicted in Figure 7A narrowed at a rate of 0.6 μm/min, similar to that of the mean rate of fiber shortening. The fibers measured within an approximate 6-μm region at the equator in sequential myosin II images were smaller than the width of the furrow and were oriented at various angles to the furrow. These measurements extend the observations of the fiber structure (Sanger *et al.*, 1994) and shortening in the furrows of dividing PtK2 cells (Sanger *et al.*, 1989). The present results suggest that contraction of fibers that transport into the cleavage furrow may constitute a second mechanism for transiently increasing the concentration of myosin II in the cleavage furrow.

2) The Myosin II Fibers Shorten as They Transport from the Equator into the Tails of the Two Forming Daughter Cells during Late Cytokinesis. The fibers transporting away from the equator during late cyto-

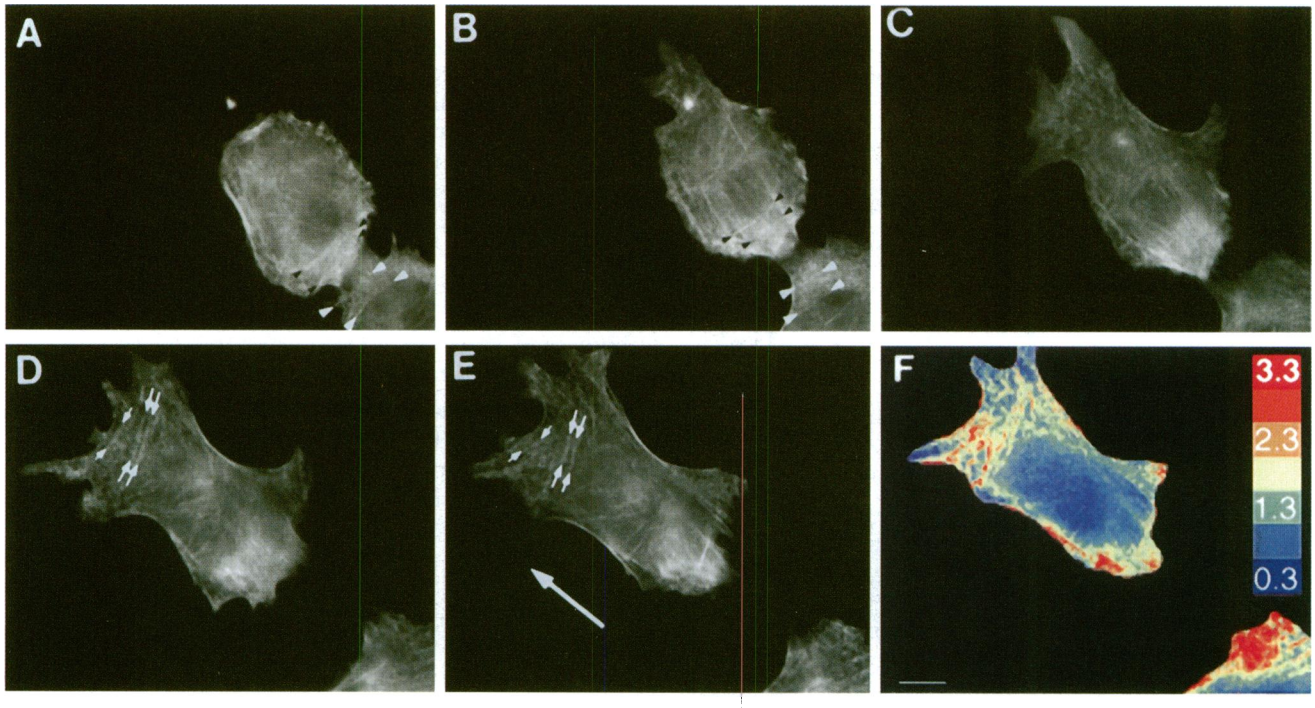

Figure 6. Myosin II fiber shortening and centripetal movement before and after cell separation. Time-lapse sequences of the myosin II, volume, VEC-DIC, and ratio images were analyzed for myosin II transport, fiber shortening, and changes in myosin II concentration during late cytokinesis and cell separation. Myosin II fibers transported away from the equatorial plane into the tails of the forming daughter cells (see also Figure 4) and shortened as they moved toward the nuclei (A and B, black arrowheads). The leading edge of each forming daughter cell ruffled and spread along the substrate as the tails of the daughter cells (cleavage furrow) narrowed. Before cell separation, the myosin II fibers in the tail regions of the daughter cells became shorter and less well-formed (C). Fibers containing myosin II (D and E, transverse fibers, small white arrows) formed at the leading edge of migrating daughter cells (large white arrow in E indicates the direction of migration). These fibers shortened and moved centripetally as the daughter cells migrated apart. Ratio images were pseudocolored, and the ratio values of the relative concentration of myosin II are represented in the color wedge in F. Ratio image analysis of the migrating daughter cells demonstrated a higher concentration of myosin II at the anterior of the cell and a lower concentration in the perinuclear region (F). Myosin II in the tail region was often elevated, but the relative concentration varied as the cell migrated and pulled the tail region forward over time. This pattern of myosin II concentration and fiber transport was comparable to the myosin II distribution seen in polarized, migrating 3T3 cells (Kolega and Taylor, 1993). Time interval between images was A, t = 0′; B, t = 17′; C, t = 27′; D, t = 37′; E, t = 49′; F, t = 50′. Bar, 13 μm.

kinesis also shorten (Figure 5, white arrowheads; Figure 6, A and B, arrowheads). Myosin II fibers shortened during transport at a relatively uniform mean rate of 0.46 μm/min (see Table 1 for statistics). The combination of the contraction of myosin II fibers in the regions between the nuclei and the furrow, and the forward migration of the leading edges of the forming daughter cells, results in the formation of the midbody and finally cell separation. Figure 6, A, B, and C, demonstrates the contraction of fibers between the nuclei and the furrow (arrowheads) and furrow narrowing. The leading edge spreads forward (Figure 6, B and C), and the daughter cells separate (Figure 6, D and E). A recoil effect in the tail region occurs after the midbody severs, and a transient, localized increase in myosin II concentration is detected in the tail region by ratio imaging (Figure 6F). A reorganization of myosin II fibers in the tail region occurs before cell separation (Figure 6C; see also Figure 8, N and U) and during the recoil period, and fewer and less well-defined myosin II fibers are detected in the tail region (Figure 6, C–E). Therefore, the transport of myosin II out of the furrow might involve the contraction of fibers into the "forming tails" of the daughter cells. This "tail contraction" during the latter stages of cytokinesis, including the separation of daughter cells, is reminiscent of the contraction in the tails of migrating cells (Kolega and Taylor, 1993).

3) Myosin II Fibers, Transverse to the Long Axis of the Dividing Cell, Shorten as They Transport Rearward after Cell Spreading Stops and Locomotion Begins. During cytokinesis, the forming daughter cells undergo a period of protrusive activity at the two "leading edges." The reorganization of myosin II (Figure 6) and reattachment to the substrate (see below, Figure 12, I–N), lasts ~15-45 min before directed locomotion of the newly formed cells usually commences. Time-lapse image sequences of myosin II

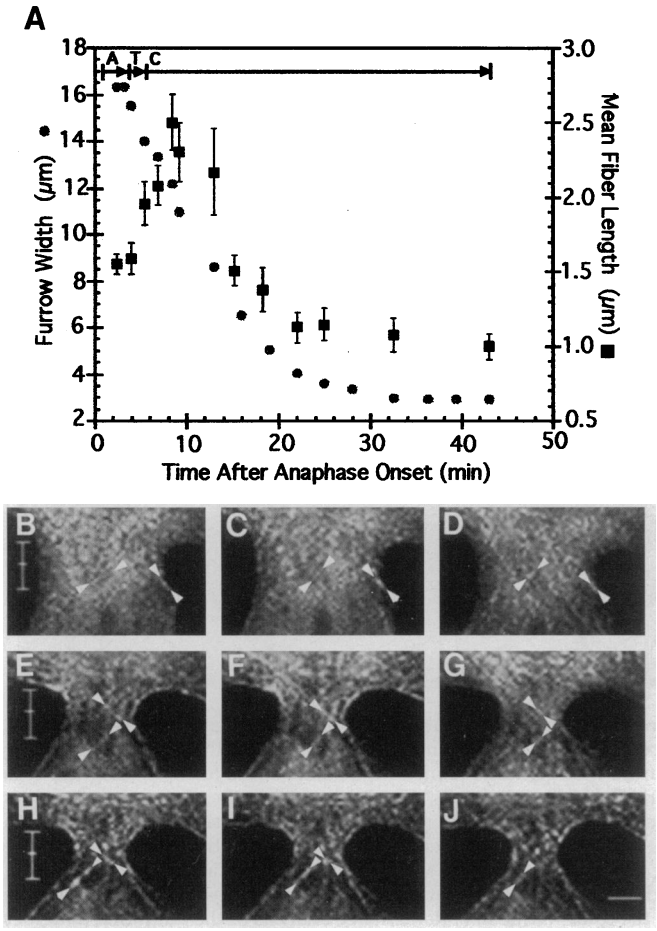

Figure 7. Myosin II fibers near the equatorial plane decreased in length during cytokinesis. Individual myosin II fibers from a representative cell that remained spread during division were measured, and their mean length (with SE bars) was plotted against time after anaphase onset. Approximately 30 fibers were measured at 14 time points during anaphase through cytokinesis. Only fibers within a defined band in the cleavage furrow (~6 μm, ~3 μm on each side of the cleavage plane) were included (see white bar in B, E, and H). The width of the furrow near the equatorial plane was also measured at the same time points. The bar at the top of the graph indicates the stages of cell division. A, anaphase; T, telophase; C, cytokinesis. Time-lapse sequences of myosin II images detected the shortening of individual myosin II fibers near the equatorial plane and in the interzone. Time-lapse sequences of myosin II images (B–D, E–G, and H–J) show the myosin II fiber organization in the region of the cleavage furrow. These myosin II images were from the same cell used to generate the graph presented in A. The ends of myosin II fibers were identified by white arrowheads. Two myosin II fibers identified in B shortened over time (C and D). Two myosin II fibers in E–G and H–J also shortened over time. The time intervals between images displayed in B–D: t = 0.00′, t = 0.75′, and t = 2.25′; in E–G: t = 0.00′, t = 0.75′, and t = 1.50′; and in H–J: t = 0.00′, t = 0.75′, and t = 2.25′. Bar, 4 μm.

demonstrate a rearward transport and shortening of fibers as they move from the anterior region of the migrating cells toward the perinuclear region. In cells that form active leading lamellae either before or after cell separation, myosin II fibers transverse to the direction of locomotion form in the lamellae, transport rearward, and contract (Figure 6, D–F). Therefore, there is a cortical flow of contracting, myosin II-based fibers from the front of the separating daughter cells to the perinuclear region. The dynamics of these transverse fibers are similar to those described in migrating 3T3 fibroblasts, polarized by the wound healing method (Kolega and Taylor, 1993; Giuliano and Taylor, 1994).

Myosin II Exhibits a Transient Increase in Concentration at the Equator during Cytokinesis

There is a transient increase in the relative concentration of myosin II at the equator starting at anaphase/telophase and peaking at mid-cytokinesis, as measured by ratio imaging of the myosin II analogue and the volume indicator. Figure 8 displays the volume indicator image series (Figure 8, A–G), the myosin II analogue image series (Figure 8, H–N), and the ratio image series (Figure 8, O–U) produced by dividing image series H–N by image series A–G. The relative myosin II concentration in the cleavage furrow increases in early anaphase (Figure 8P), peaks in mid-cytokinesis (Figure 8S), and decreases during late cytokinesis as the width of the cleavage furrow decreases to form the midbody (Figure 8, T and U). The ratio imaging results are also consistent with two-dimensional, time-lapse transport data that demonstrate a transient gain of myosin II in the furrow (Figures 3–5), as well as the fiber shortening (contraction) data that indicate this second mechanism for a transient elevation of myosin II concentration in the furrow (Figures 4–6).

The ratio imaging of the whole cell allows global changes in the relative myosin II concentration to be analyzed rapidly. The increase in myosin II concentration at the leading edge of the spreading daughter cells occurs in parallel with the onset of cytokinesis (Figure 8R) and continues through the spreading stage and locomotion of the still-attached daughter cells (Figure 8U). Thus, the dividing cell begins to reorganize the contractile machinery for polarized locomotion of the daughter cells, in parallel to the onset of cytokinesis.

Phosphorylation of the Myosin II Regulatory Light Chain at Serine 19 Exhibits a Temporal–Spatial Pattern that is Consistent with the Transport and Contraction Dynamics

The spatial relationship between the phosphorylation of myosin II RLC at serine 19 and the relative concentration of myosin II was determined by performing dual ratio measurements using CB-dex-10K and the combined, fluorescein and rhodamine myosin II fluorescent analogue and biosensor for phosphorylation

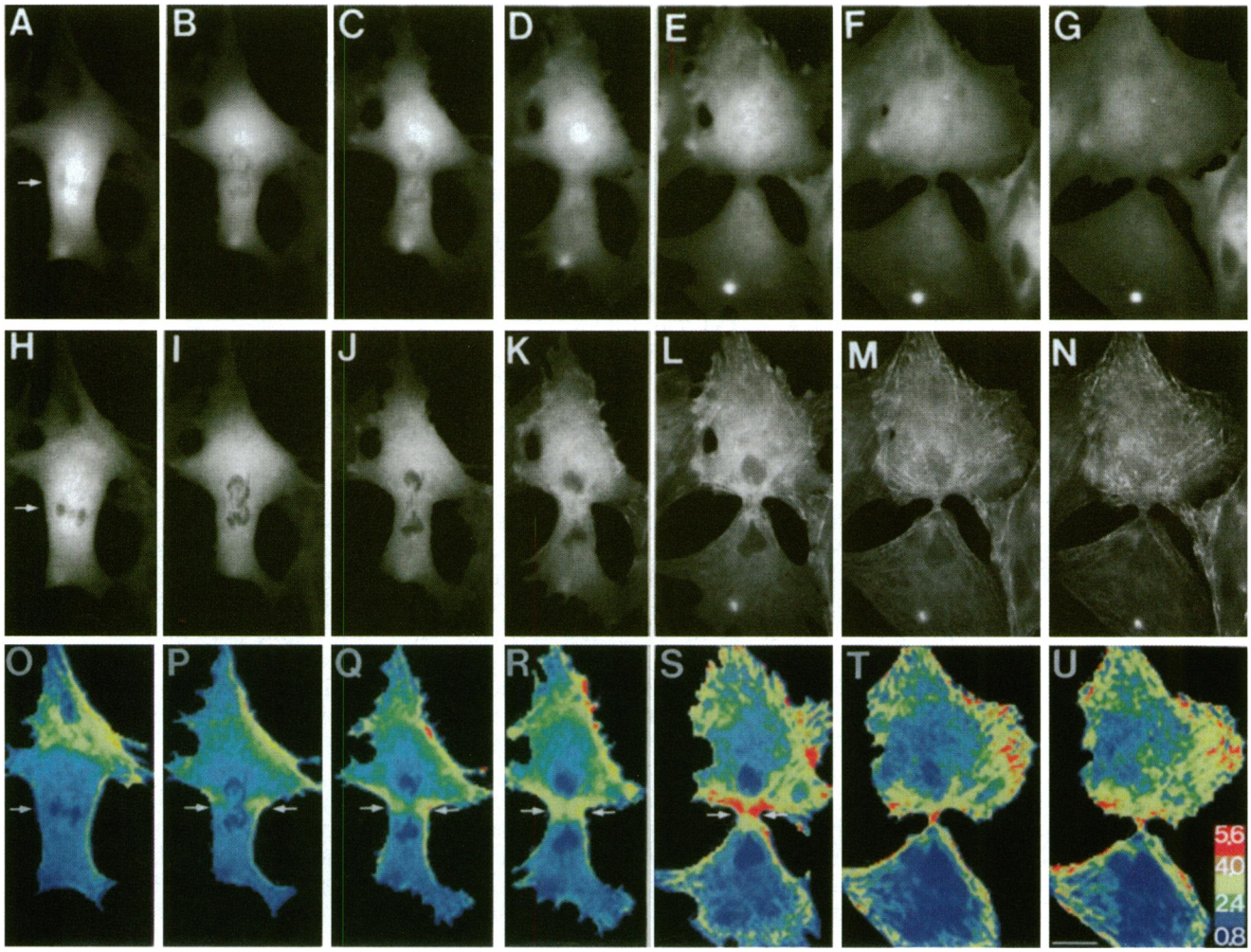

Figure 8. Transient increase in the concentration of myosin II in the cleavage furrow during cytokinesis. Multimode time-lapse image sequences of 3T3 fibroblasts undergoing division were collected during prometaphase through late cytokinesis. The VEC-DIC sequence, not shown, was used to determine the stage of cell division. The volume indicator sequence A–G and the corresponding myosin II images H–N were used to generate the myosin II ratio image series O–U by dividing the myosin II images by the corresponding volume images. The ratio images were pseudocolored, and the ratio values of the relative concentration of myosin II are given in the color wedge (U). Image A was acquired during prometaphase; B, anaphase; C, telophase; and D–G, early-to-late cytokinesis. The volume indicator image showed that the region near the chromosomes during prometaphase (A, arrow) and metaphase had the largest path length and accessible volume before anaphase. The myosin II fluorescence intensity observed in this area (A and H, arrows) was due to the accessible volume in this region and not to specific myosin II concentration. This was confirmed by the ratio image (O, arrow), which showed a relatively low uniform distribution of myosin II near the chromosomes. Changes in regions of myosin II concentration could be determined only from the ratio-image sequences. An elevated concentration of myosin II near the equatorial plane was observed during anaphase (P, arrows). The concentration of myosin II increased in the interzone and regions adjacent to the interzone during telophase (Q) and early cytokinesis as the furrow width narrowed (R and S). The concentration of myosin II in the midbody and the rear or tails of the forming daughter cells decreased during late cytokinesis (T and U). An elevated concentration of myosin II in the peripheral cell regions was detected over time during cytokinesis (R–U) as the furrow width narrowed and the forming daughter cells spread along the substrate. Time intervals between images were A, t = 0.00′; B, t = 8.00′; C, t = 10.25; D, t = 12.75′; E, t = 21.50′; F, t = 36.50′; G, t = 51.50′. Bar, 19 μm.

(Figure 9). The pseudocolor maps are scaled within each image to optimize the visualization of the spatial patterns. Therefore, no comparisons of amplitudes can be made between the pairs of images at different stages of division in Figure 9. Cells in prometaphase (7 of 7 cells) exhibited a spatially uniform myosin II concentration (Figure 9A) and level of phosphorylation (Figure 9B), and in metaphase (3 of 3 cells) showed the same pattern (our unpublished results). Cells in anaphase showed either a spatially uniform myosin II concentration and level of phosphorylation (3 of 7 cells), or a slight elevation of both at the equator (4 of 7 cells) (Figure 9, C and D). Cells in telophase (4 of 4 cells) exhibited an elevation of myosin II concen-

tration and phosphorylation at the equator (Figure 9, E and F). The close correlation between elevated myosin II concentration and phosphorylation in the cleavage furrow continued in cytokinesis (12 of 12 cells) (Figure 9, G and H). The spatial domain of elevated phosphorylation was always larger than the domain of elevated concentration of myosin II. The region of elevated phosphorylation between the chromosomes or the reforming daughter nuclei (Figure 9, F and H) corresponds to the spatial domain exhibiting the maximal-directed transport and shortening (contraction) of fibers containing myosin II (Figures 3, 4, 6, and 7). The pattern of phosphorylation supports the interpretation of the fiber shortening as a contraction (see DISCUSSION).

The concentration and phosphorylation of myosin II varied in the tail regions based in part on the timing of image acquisition relative to tail retraction and the stage of polarization of the cell after cell separation (Kolega and Taylor, 1993; Post *et al.*, 1995). Migrating cells (generated by wound healing) that became fully polarized exhibited a clear gradient of myosin II phosphorylation of the RLC at serine 19, with a maximum in the tail (Post *et al.*, 1995). The leading edge of daughter cells, migrating during and after cell separation, showed a gradient of myosin II concentration, highest near the leading edge and lowest in the perinuclear region exactly like migrating cells during wound healing (Figure 9I) (Kolega and Taylor, 1993). Maximal phosphorylation of myosin II RLC did not match the spatial pattern of myosin II concentration at the leading edge of daughter cells migrating during and after cell separation. Elevated myosin II phosphorylation was detected in transverse fibers posterior to the leading edge (Figure 9J, black arrowheads), where they are known to transport in the retrograde direction while shortening (contracting) (Kolega and Taylor, 1993; Post *et al.*, 1995).

Time-lapse studies using the myosin II phosphorylation indicator demonstrated a global rise in the phosphorylation of the myosin II RLC at serine 19, starting in anaphase (Figure 10, A–C). This is consistent with the timing of the initiation of directed transport of myosin II into the equator and the elevation of myosin II concentration in the equator (Figures 3–8). The phosphorylation of myosin II RLC at serine 19 is maximal at the site of the forming cleavage furrow in telophase (Figure 10D) and continues with the same pattern into early cytokinesis (Figure 10E), when the level of phosphorylation begins to decrease. Myosin II phosphorylation of the RLC at serine 19 continues at a slightly elevated level in the furrow late in cytokinesis, while also beginning to increase near the active leading edges of spreading daughter cells (Figure 10F, arrowhead). The temporal–spatial pattern of myosin II phosphorylation of the RLC at serine 19 is consistent with the temporal–spatial patterns of myosin II transport and contraction. This is the first direct evidence of the activation of myosin II as part of the process of cytokinesis. The temporal dynamics reported here are also consistent with the timing of the phosphorylation of myosin II RLC at serine 19 characterized by Yamakita *et al.* (1994), however, this study adds the dynamic, spatial information missing in bulk biochemical methods (Post *et al.*, 1995).

The Three-Dimensional Organization of the Myosin II Fibers in the Cleavage Furrow Demonstrates that the Cleavage Furrow Is More Complicated than a Purse-String

The three-dimensional organization of the myosin II analogue was defined as a function of the stage of cell division. This is the first molecularly specific characterization of the three-dimensional structure of the cleavage furrow in a living cell. A single, three-dimensional image stack of a living cell could be acquired without causing noticeable damage, as judged by comparing the myosin II organization in a few optical sections taken at the lower, center, and upper focal plane from a dividing cell, with image stacks using a 0.2-μm spacing taken at a similar phase of division in other dividing cells. Extended time-lapse three-dimensional stacks were not analyzed to minimize photo damage and to ensure the physiological significance of the data. Therefore, three-dimensional image stacks were usually acquired from separate cells in each stage of cell division. A punctate fluorescence of myosin II was observed from metaphase to late cytokinesis (Figure 11) and is consistent with a filamentous state of myosin II (Fukui, 1993; Kolega and Taylor, 1993; Verkhovsky and Borisy, 1993; Maupin *et al.*, 1994). A fairly uniform distribution of punctate myosin II was detected both at the poles and near the equator during metaphase (Figure 11, A–E) and early anaphase (Figure 11, F–J). This distribution was present throughout the volume of the cell, with the exception of a slight concentration near the chromosomes in the central planes of the cells (Figure 11, C and H, arrows). Cells in prometaphase showed the same uniform distribution of punctate myosin II throughout the cell, but some cells also had a few long myosin II fibers near the cell periphery that disappeared by metaphase (our unpublished results). The presence of punctate myosin II fluorescence even during prometaphase and metaphase, when the myosin II phosphorylation of the RLC at serine 19 is low (Figure 10) (Yamakita *et al.*, 1994), suggests that the regulation of myosin II assembly and activation of the motor are distinct events (Kolega and Taylor, 1993; Post *et al.*, 1995).

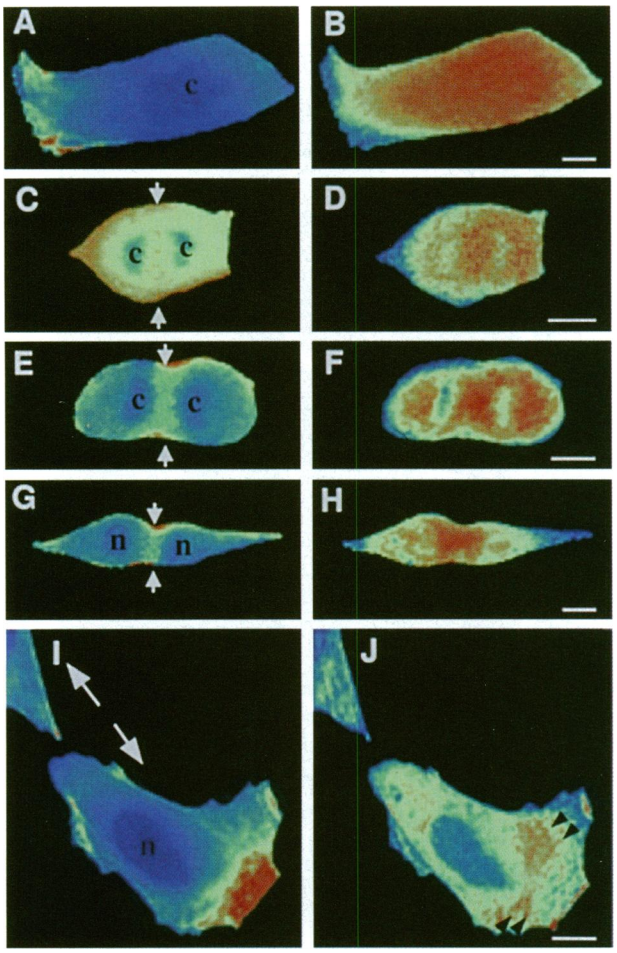

Figure 9. Spatial distribution of myosin II and myosin II phosphorylation of RLC in dividing fibroblasts. Interphase 3T3 fibroblasts were microinjected with a mixture of the volume indicator Cascade Blue dextran 10K and the fluorescein- and rhodamine-labeled biosensor for myosin II phosphorylation of the RLC at serine 19. A single, rapid sequence of the CB-dex-10K volume image, the fluorescein– and rhodamine–myosin II phosphorylation biosensor, and VEC-DIC and RIM images were acquired at a specific phase of cell division. In all, 43 cells were studied either at prometaphase (n = 7), metaphase (n = 3), anaphase (n = 7), telophase (n = 4), cytokinesis (n = 12), or after cell separation (n = 10). Myosin II ratios were generated by dividing the rhodamine myosin II image by the CB-dex-10K volume image, and the myosin II phosphorylation ratio was generated by dividing the rhodamine myosin II image by the fluorescein RLC image. Each ratio was scaled independently to enhance visualization of the spatial distribution of the myosin II concentration and myosin II phosphorylation level; hence, no correlation between the maximal ratio values between the myosin II concentration and phosphorylation level or between individual cells can be made (high-ratio values are represented in red; lower-ratio values are represented in blue). The spatial pattern of myosin II phosphorylation varied (see RESULTS), but representative cells were displayed. A relatively uniform pattern of myosin II concentration and myosin II phosphorylation was observed in prometaphase (A and B) and metaphase. When the concentration of myosin II increased near the equatorial plane (arrows) during anaphase (C), telophase (E), and cytokinesis (G), the myosin II phosphorylation indicator demonstrated maximal phosphorylation in the cleavage furrow (D, F, and H). After cell separation (I and J), when the

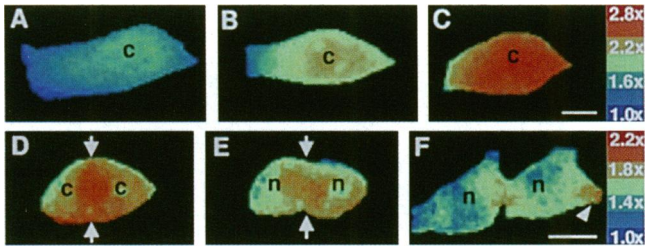

Figure 10. Temporal changes in myosin II phosphorylation during cell division. Interphase cells were microinjected as described in Figure 9, and the same sequence of images was acquired. However, in this study, second and third series of images were acquired on the same cell as it proceeded through cell division. In all, 15 cells were studied for temporal changes in phosphorylation of serine 19 of myosin II during division. During the three time points of acquisition, photobleaching of the rhodamine myosin II images was negligible, but the fluorescein myosin II images were corrected for photobleaching (see MATERIALS AND METHODS). The series of the three ratios were internally scaled, and the ratio wedge shown in the last image applies to the images in that sequence. The ratios were pseudocolored for visual enhancement, and the ratio values were presented as a fold response from the lowest ratio value in the series (given the value of 1.0 and represented in blue) to the maximal level of response (given as a factor fold increase and represented in red). The first time-lapse sequence showed a representative cell during early prometaphase (A), metaphase (B), and at anaphase onset (C). The phosphorylation biosensor demonstrated a global rise in myosin II phosphorylation as the cell entered into anaphase. Another cell (D–F) was examined in telophase (D), early cytokinesis (E), and a later stage of cytokinesis (F). Myosin II phosphorylation was localized in the interzone during telophase and cytokinesis (see Figure 9, F and H), but the relative level of myosin II phosphorylation decreased in the cleavage furrow over time (arrows in D and E indicate the equatorial plane). Areas of elevated myosin II phosphorylation were also observed in actively spreading regions of the forming daughter cell (F, arrowhead). c, chromosomes; n, nucleus. Bar, 16 μm.

An increased concentration and fiber organization of myosin II was detected near the equator during anaphase and telophase (Figure 11, K–R), whereas the more polar regions continued to express a more random, punctate structure of myosin II. The fibers were detected throughout the interzone, from the ventral to dorsal regions of the cell, with a denser distribution in the central region of the interzone (Figure 11, M and Q). During telophase (Figure 11, O–R), fibers in the interzone became longer and were oriented both parallel and perpendicular to the plane of the cleavage

(Fig. 9 cont.) daughter cells migrated apart, a gradient of higher myosin II concentration was determined near the leading edge, with a decreasing concentration toward the nucleus (white arrows in I indicate the direction of migration). The myosin II phosphorylation level was lower at the leading edge of locomoting daughter cells, with higher levels in the contracting, transverse fibers (J, black arrowheads). The pattern of myosin II concentration and phosphorylation at the leading edge and the tail varied, depending on the activity of the daughter cell as it spread, retracted, or locomoted; c, chromosomes; n, nucleus. Bar, 12 μm.

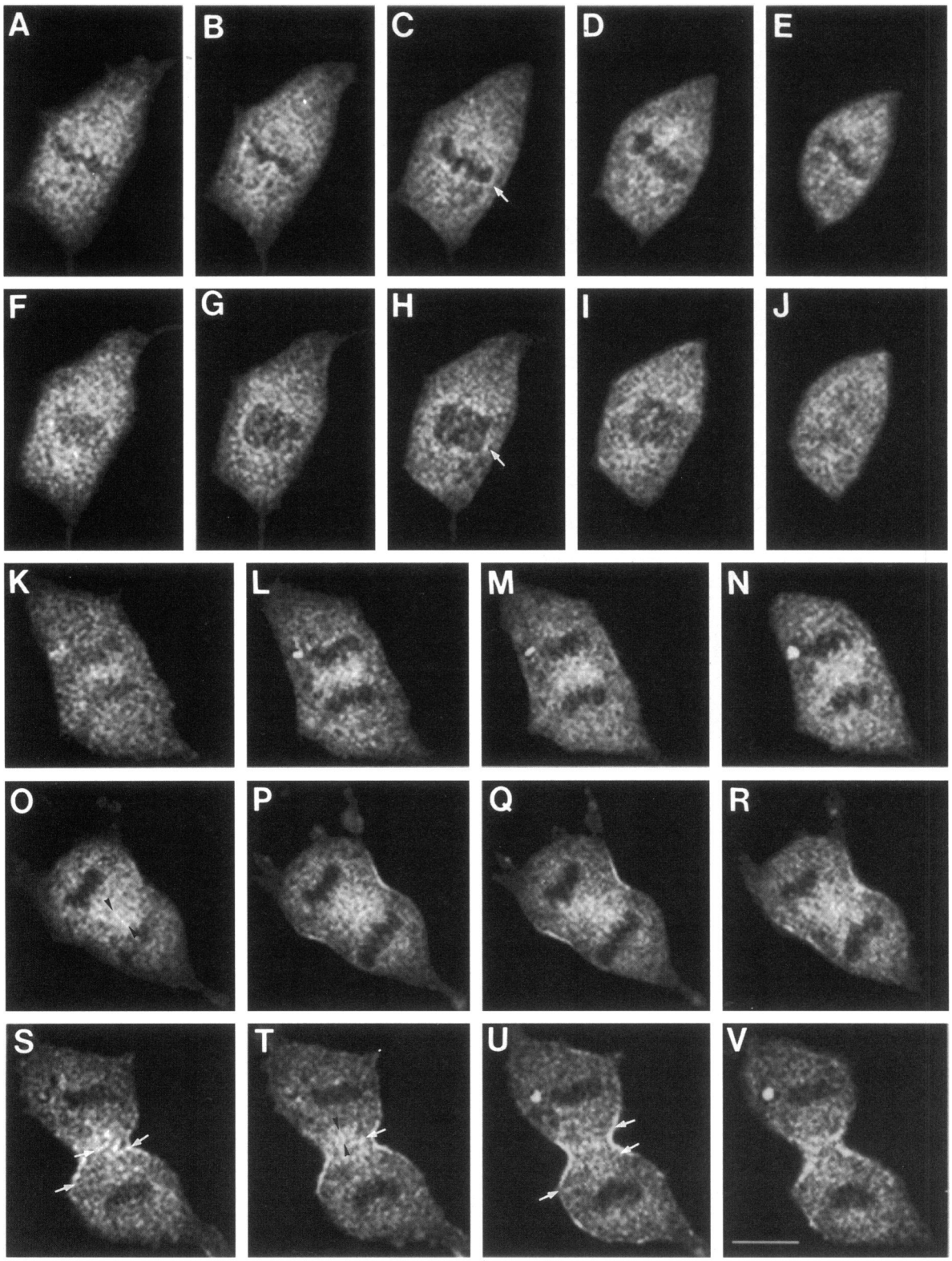

Figure 11. Three-dimensional organization of fibers containing myosin II in live 3T3 fibroblasts during cell division. Three-dimensional optical sections of AR-myosin II-microinjected cells were taken at different stages during division. Three-dimensional stacks were deconvolved using the nearest-neighbor algorithm (see MATERIALS AND METHODS) and then sharpened to enhance detail. A fairly uniform

furrow. A similar organization of actin fibers was observed in cells fixed and labeled with rhodamine-phalloidin (Cao and Wang, 1990a). The three-dimensional organization and concentration of myosin II is also consistent with the two-dimensional time-lapse data that demonstrated a transient concentration of myosin II in the interzone based on the transport of fibers containing myosin II into the furrow region and their contraction (Figures 3–6 and 8). The increased number of short fibers containing myosin II throughout the volume of the interzone during anaphase and telophase demonstrated the complex three-dimensional organization of myosin II in the cleavage furrow.

The Furrow Region Loses Contact with the Substrate during Early Cytokinesis as the Furrow Width Narrows

RIM analysis of membrane contact with the substrate is a sensitive indicator of cell adhesion and detects membrane-to-substrate association within nanometers of the substrate. Cycling 3T3 fibroblasts maintain regions of focal and close contact with the substrate (Bereiter-Hahn *et al.*, 1979). Focal contacts were observed when the ventral cell membrane was strongly attached to the substrate. Focal contacts have previously been determined to indicate that the membrane was <10 nm from the substrate, and close contacts were observed when the membrane was within 10–30 nm of the substrate (Bereiter-Hahn *et al.*, 1979). Time-lapse analysis of RIM, myosin II, and volume images of 3T3 fibroblasts showed that during prophase and prometaphase, myosin II-based stress fibers disappeared, and focal contacts were lost, but regions of close contact remained as cell motility decreased and the peripheral cell edges retracted (our unpublished results). Cells that remained spread along the substrate during cell division (Figure 12, A–H) had more regions of close contact than those that had rounded (Figure 1B). However, all 3T3 fibroblasts displayed only minimal points of close contact during cell division, and therefore all 3T3 fibroblasts are weakly attached to the substrate when compared with the numerous regions of focal and close contact present in these cells before the onset of mitosis. Burton and Taylor (unpublished data) noted that traction forces generated by fibroblasts during cell division on SILASTIC sheets were weaker than the forces generated by pre- and postmitotic motile cells.

During late prometaphase to telophase, close contacts were observed in various locations in the central region of the cell (Figure 12, A–H). No close contacts at the polar regions were observed during prometaphase to telophase. In some cells, close contacts were not present at the equator, indicating that the ventral surface of the cell near the equator was >30 nm above the substrate during prometaphase to telophase. When close contacts were located near the equator before telophase (Figure 12D, arrow), most of the contacts were lost during anaphase and telophase as the chromosomes separated and condensed (Figure 12F, arrow). The equatorial region that formed the midbody during late cytokinesis (Figure 12, I and J, short black arrow) did not re-form close contacts to the substrate until after the midbody severed (Figure 12, K and L), and the cells separated (Figure 12, M and N).

DISCUSSION

Cleavage Furrow Formation Involves Myosin II Transport, Phosphorylation, and Contraction

Historically, the question of how the cleavage furrow forms has been addressed at two levels of organization: 1) the global regulation of the site of cleavage, and 2) the molecular details about how actin, myosin II, and other proteins become transiently concentrated in the equatorial region that forms the cleavage furrow. Our results give important insights at both levels. The polar relaxation model predicts that the actin and myosin II in the cortex would transport globally toward the equator because of a relative relaxation at the poles (White and Borisy, 1983), whereas the equatorial stimulation model predicts that the furrow would be stimulated (activated) to form at the equator by a local stimulus arising from the spindle (Rappaport, 1971). Our results on the directional transport of myosin II from a region adjacent to the equator into the forming furrow (Figure 3 and Table 1) are consistent with previous results using labeled actin filaments (Cao and Wang, 1990a,b) and fluorescent tracer particles (Wang *et al.*, 1994), as well as Con A (Koppel *et al.*, 1982) on the cell surface. There is evidence for cortical flow of actin and myosin II into the furrow. However, the transport was not uniform from the poles to the equator in the more adherent, flattened cells that were investigated in detail (Figure 3). Most of the directed

(Figure 11 cont.) distribution of punctate myosin II was detected throughout all images of the three-dimensional stack during prometaphase (our unpublished results), metaphase (A–E), and anaphase onset (F–J). A slight localization of punctate myosin II was observed in the center planes of cells in metaphase and anaphase onset (C and H, arrow). An increased localization and organization of fibers containing myosin II were detected in the interzone during anaphase (K–N) and telophase (O–R). Fibers became more distinct and lengthened during telophase (O–R) and were oriented both parallel and perpendicular to the equatorial plane. During cytokinesis (S–V), numerous myosin II fibers throughout the volume of the interzone were detected parallel to the equatorial plane (arrows in S, T, and U indicate some of these fibers). Fibers perpendicular to the equatorial plane (T, black arrowheads) and at various angles to the equatorial plane were also detected throughout the volume of the cleavage furrow in three-dimensional sections during cytokinesis. Bar, 13 μm.

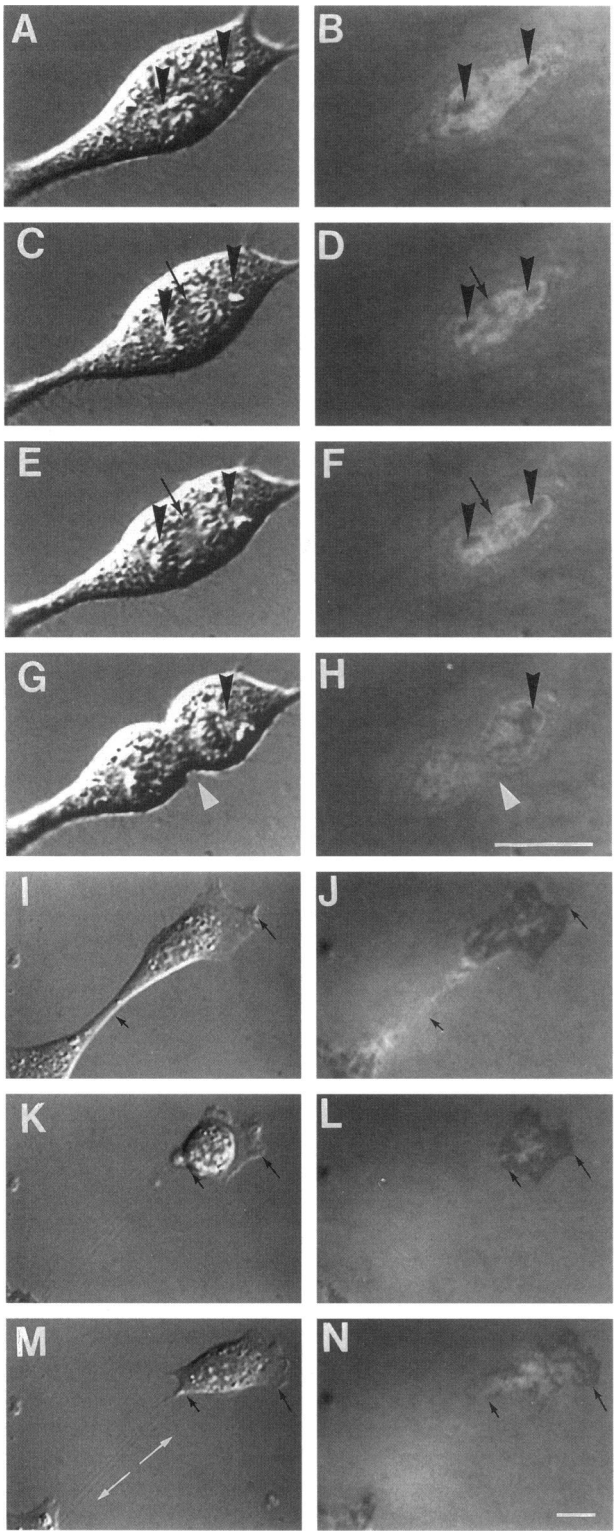

Figure 12. Substrate attachment during cell division. Time-lapse sequences of VEC-DIC and RIM demonstrated the interaction of 3T3 fibroblasts with the substrate during cell division and the migration of daughter cells. Although there was some variability between cells, this data set is representative of the dynamic changes observed in most cells. During prometaphase (A and B) through anaphase (C and D), telophase (E and F), and early cytokinesis (G and H), no focal contacts were observed, but regions of close contact were located primarily in the central areas of the cell (A–H, black arrowheads) with few or no close contacts at the peripheral cell edges. In some cells, close contacts were detected near the equatorial plane before telophase (C and D, black arrow), but diminished or were lost during telophase (E and F, black arrow). After early cytokinesis, no regions of contact with the substrate were observed in the furrow (G and H, white arrowhead). During late cytokinesis, the midbody remained distant from the substrate (I and J, short black arrow) as the forming daughter cells spread, reestablished close contacts with the substrate, and began to migrate apart. The leading edge of the forming daughter cells formed a broad region of close contact with the substrate (I and J, long black arrow). After forward migration, the midbody severed and the tail region retracted (K and L, short black arrow) and recoiled toward the close contacts located in the anterior region of the cells. The leading edge of daughter cells formed close contacts behind the regions of active lamellipodia (M and N, long black arrow), and the cells migrated apart. During cell locomotion, fewer regions of close contact were located in the tail region (N, short black arrow). White arrows in M indicate the direction of cell migration. Bars, 16 μm.

transport was detected from regions adjacent to the equator into the cleavage furrow, which is not predicted from the simplest interpretation of the polar relaxation model. Attachment of fibroblasts to the substrate, albeit weak (Figure 12), may modulate the cortical flow or transport of actin and myosin II compared with the dynamics of cytokinesis in systems such as embryos of sea urchins and *C. elegans* (Hird and White, 1993). Our results are consistent with elements of both the polar relaxation and the equatorial stimulation models, but the detailed mechanism of the global regulation of cytokinesis will require further investigation.

The movements of myosin II in all directions at the poles during anaphase and telophase, with directed transport near the furrow (Figure 3), is consistent with the production of global, cortical contractions. Therefore, the poles are not simply relaxing, but instead global cortical contractions are occurring during cytokinesis (Dan, 1954; Rappaport, 1986; Wang *et al.*, 1994). We have recently detected and measured traction forces being applied at a pole of a dividing cell, simultaneous with forces generated at the equator during cleavage furrow formation (Burton and Taylor, unpublished data). Also, our data using the biosensor of phosphorylation (Figures 9 and 10) further demonstrate that the activation of myosin II initially occurs globally and that activation remains at the highest level in the cleavage furrow. Therefore, the activation is not limited to the cleavage furrow as predicted by the simplest interpretation of the equatorial stimulation model, but is maintained in the furrow for a longer period of time than the polar region. The simplest explanation of these and previous results is that cleavage is initially signaled by global activation of the cortex, followed by regulatory events that transiently

maintain the contractile stimulus in the cleavage furrow while allowing the decay away from the furrow. This may involve a regulated pattern of controlling the phosphorylation of the inhibitory sites of myosin II (ser 1 and 2 and possibly thr 9) vs. the activation site (serine 19) of RLC phosphorylation (Satterwhite and Pollard, 1992; Yamakita *et al.*, 1994). Controlling the temporal–spatial dynamics of inhibitory kinases for myosin II, such as $p34^{cdc2}$ kinase (Lamb *et al.*, 1990; Satterwhite and Pollard, 1992), may be as important to patterning the cleavage furrow dynamics as the activation kinase, myosin light chain kinase (Fishkind *et al.*, 1991; Yamakita *et al.*, 1994). Thus, the spindle may play a more important role in maintaining the myosin II "activation" state than actually initiating the process.

The transient increase in myosin II concentration in the cleavage furrow appears to involve at least two mechanisms: 1) the transport of myosin II from adjacent regions, and 2) the contraction of the myosin II-based fibers in the cleavage furrow (Figures 3–6, 9, and 10). Our results do not exclude local assembly of myosin II in the furrow, but previous results with actin (Cao and Wang, 1990a,b) suggest that most of the elevation of actin in the furrow is caused by transport. The active contraction of myosin II-based fibers in the furrow region (Figures 4–10) also contributes to the increased, but transient density of myosin II in the furrow.

The Dynamics and Structure of the Cleavage Furrow Provide Insights about the Possible Mechanisms of Force Production

Three possible mechanisms for force production have been discussed based on the prevailing models of the structure of the cleavage furrow (Fishkind and Wang, 1995). The purse string model suggests that a circumferential band of actin and myosin II filaments "constricts" the dividing cell into two daughter cells, the isotropic contraction model suggests that cleavage is achieved by the contraction of a random network of actin and myosin II, and the traction model predicts that tension applied to the membrane, but extending into the cytoplasm of the forming daughter cells, would pull the membrane inward to form the furrow. The two-dimensional transport data (Figure 3), the sites of contraction (Figures 4–7, 9, and 10), and the three-dimensional organization of the forming and contracting furrow (Figures 1 and 11) demonstrate that the mechanism of force production involves elements of each of the possible mechanisms. The early transport of myosin II forms isotropic arrays of myosin II fibers throughout the volume of the forming furrow. Distinct, anisotropic fibers became evident both parallel and perpendicular to the plane of the furrow from telophase into early cytokinesis as contractions are initiated. The formation of anisotropic fibers is probably due to the application of forces to a "gelled" actin network by the myosin II motors (Taylor *et al.*, 1973; Condeelis and Taylor, 1977; Janson and Taylor, 1993). This interpretation is consistent with the structures defined in the cleavage furrows of fixed, dividing cells using fluorescence anisotropy and three-dimensional fluorescence of rhodamine-phalloidin, labeled actin (Fishkind and Wang, 1993), as well as the patterns of birefringence in the equator of dividing cells (Fukui and Inoue, 1991). Furthermore, tension wrinkles form transiently at the cleavage furrow in cells dividing on rubber sheets (Burton and Taylor, unpublished data). These wrinkles form during the early phase of cytokinesis when the myosin II fibers are contracting into the furrow (Figures 6 and 7), and anisotropic fibers are observed both parallel and perpendicular to the plane of the furrow.

Forces are subsequently propagated into the cytoplasm of the forming daughter cells as the direction of transport of myosin II fibers reverses and the fibers transport toward the rear of the forming daughter cells, while also contracting (Figure 6, A–C). Therefore, the later stages of cytokinesis involve the retraction of myosin II out of the furrow, toward the reforming nuclei in the tails. The ability to detect and measure the dynamics of the cleavage furrow has resulted in defining a dynamic sequence consisting of forming the initial structures primarily by transport, creating anisotropic arrays by initial contraction and then removing the furrow by both retrograde transport of the fibers and a self-destructing contraction, forming the tails of the forming daughter cells (Janson and Taylor, 1993; Kolega and Taylor, 1993). Figure 13 depicts the dynamic events of myosin II in cytokinesis.

The Cortical Flow/Solation–Contraction Coupling Mechanism in Cell Division and Polarized Cell Locomotion

It is clear from comparing the temporal–spatial dynamics of the organization, transport, regulation, and contraction of myosin II fibers during cytokinesis and polarized cell locomotion of the same cell type (Hahn *et al.*, 1992; Kolega and Taylor, 1993; Post *et al.*, 1995) that there is a continuum in the mechanisms responsible for these two cellular processes. A possible relationship between cell locomotion and cytokinesis has been suggested previously (for review, Swann and Mitchison, 1958; Taylor and Fechheimer, 1982; Bray and White, 1988; Janson and Taylor, 1993). Final cell separation at the conclusion of cytokinesis yields two daughter cells that exhibit patterns of rearward transport of transverse fibers, the contraction of the transverse fibers as they transport toward the nucleus, and the gradient of myosin II RLC phosphorylation, low at the leading edge and increasing posteriorly toward

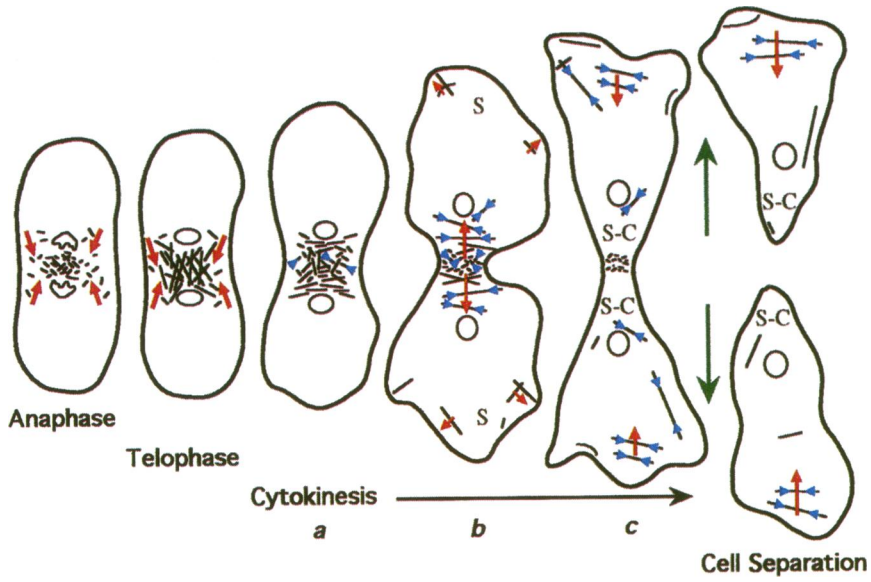

Figure 13. Summary diagram of the transport and shortening of fibers containing myosin II during cell division. The results support a cortical flow/solation–contraction coupling mechanism of cytokinesis. Black lines within the cell represent fibers containing myosin II. Red arrows indicate the direction of fiber transport. Blue arrowheads show fiber shortening. Green arrows indicate the direction of migration. Temporal changes during cytokinesis are labeled *a*, *b*, and *c*. S, spreading cell edges; S–C, solation–contraction sites in the tails of forming and separated daughter cells. See DISCUSSION for an overview of the cortical-flow/solation–contraction coupling mechanism of cell division and polarized cell locomotion.

the nucleus, similar to that of polarized, migrating cells (Figures 6 and 9). There is now more information about gradients and/or patterns involved in the polarized, migration of cells compared with cytokinesis, although this gap is narrowing. Fully polarized migrating cells also exhibit the following gradients: 1) actin incorporation at the leading edge (Wang, 1985; Giuliano and Taylor, 1994); 2) myosin II concentration maximal at the base of lamellipodia in transverse fibers and lowest in the perinuclear region (Conrad *et al.*, 1993; Kolega and Taylor, 1993); 3) free calcium ion concentration and calmodulin activation maximal in the tail (Hahn *et al.*, 1992); and 4) phosphorylation of the myosin II RLC at serine 19 maximal in the tail (Post *et al.*, 1995). Setting up these unipolar gradients in single, migrating cells is related to the creation of bipolar cells during earlier stages of cell division.

The following mechanism for cytokinesis of motile animal cells attached to substrates is consistent with the available data. It has been well-established that cytokinesis can occur in most, if not all, animal cells without the need for attachment to the substrate (Rappaport, 1986) unless the myosin II motor is knocked out (DeLozanne and Spudich, 1987). However, Swiss 3T3 cells grown in culture not only take advantage of the substrate to complete the separation process, but the patterns of transport, regulation, and contraction of the dividing cells are similar to those of single migrating cells.

The major steps in cytokinesis of Swiss 3T3 cells from anaphase through the separation of the daughter cells are depicted in Figure 13. The proposed model integrates previous concepts of cortical flow (Bray and White, 1988) and solation–contraction coupling (Taylor and Fechheimer, 1982; Janson and Taylor, 1993; Kolega and Taylor, 1993; Giuliano and Taylor, 1994; Post *et al.*, 1995), as well as the rich history of research on cytokinesis (for review, Fishkind and Wang, 1995). The model deals with the role of only myosin II as a molecular motor, although other motors may play important roles (Breckler and Burnside, 1994). Moreover, there is no attempt to integrate the possible role of the spindle in localizing the contractile events (Rappaport, 1971; Fishkind and Wang, 1995), although this appears to be an important aspect of regulating cell division.

Starting in anaphase, a cortical transport of actin/myosin II into the equatorial plane forms a three-dimensional isotropic network that also contains other cytoskeletal and regulatory components (Cao and Wang, 1990a; Fishkind and Wang, 1993; Wang *et al.*, 1994) (see also Figure 13, anaphase). A global activation of myosin II, via the phosphorylation of the RLC at serine 19, initiates the contractile events. A gradient of RLC-activating phosphorylation is optimally patterned during telophase so that the phosphorylation is maximal at the equator and lower at the poles (Figures 9H, 10D, and 13, telophase). This pattern of phosphorylation (Figures 9 and 10) creates a bipolar dividing cell. The equator can now be viewed as forming the two tails of the daughter cells. Maximal contraction at the equator generates tension in the gelled cytoplasm that causes the formation of fibers, both perpendicular and parallel to the plane of the furrow (Figures 3–6, 8, and 13, telophase and cytokinesis [*a*]) (Fukui and Inoue, 1991; Fishkind and Wang, 1993). The latter stages of contraction involve forces directed into the tails of the forming daughter cells as the cleavage furrow lifts from the substrate and the cells begin to separate (Figure 13, cytokinesis [*b* and *c*]).

The contracting tail fibers in each daughter cell disappear near the re-forming nuclei (Figures 6 and 13, cytokinesis [*c*]). The simplest interpretation of the loss of fibers is that a self-destruct, solation–contraction coupling occurs to generate the force needed to take apart the cleavage furrow and recycle the contractile units in a controlled process (Taylor and Fechheimer, 1982; Janson *et al.*, 1991; Kolega *et al.*, 1991; Janson and Taylor, 1993; Kolega and Taylor, 1993; Giuliano and Taylor, 1994; Post *et al.*, 1995). In parallel with the contraction of some of the fibers in the cleavage furrow that produce a force directed forward into the tails, there is a transport of both actin (Cramer and Mitchison, 1995) and myosin II (this study) into the advancing edges of the spreading daughter cells (Figure 13, cytokinesis [*b*]). The subunits incorporated in the front of the two daughter cells may be made available from the self-destructing contractions in the tails. The model therefore predicts that dephosphorylation of myosin II RLC at serine 19 would generate 10s myosin II monomers that could be recruited into the forming, actin-based cytoskeleton near the leading edge (Kolega and Taylor, 1993). The apparent dichotomy of maximizing activation and deactivation of myosin II in a short span of time and in the same region of the cell is actually a necessary feature of cytokinesis and polarized cell locomotion. The dividing cell must develop contractile force at the equator without creating a large contracted domain at the end of cytokinesis, and the polarized, locomoting cell must generate contractile force in the cortex, maximal in the tail, and then cycle the contracted components back into subunits for assembly at the leading edge. Therefore, maximal activation must be coupled sequentially with deactivation and recycling. This is one of the key features of the solation–contraction coupling mechanism (Taylor and Fechheimer, 1982; Janson *et al.*, 1991; Kolega *et al.*, 1991; Janson and Taylor, 1993; Kolega and Taylor, 1993; Giuliano and Taylor, 1994; Post *et al.*, 1995).

The retraction of the separating tails can aid in the redistribution of the subunits to the leading edges of the daughter cells (Kolega and Taylor, 1993; Giuliano and Taylor, 1994; Post *et al.*, 1995). This cycle, or flow, of actin filaments and myosin II into the furrow and their subsequent transport to the leading edges of the daughter cells is a central part of the cortical flow hypothesis (Bray and White, 1988; Cao and Wang, 1990b). The actin and myosin II incorporated into the leading edges of the daughter cells play a role in defining the polarity of the daughter cells, front to tail. Even before the daughter cells separate, the rearward transport of transverse fibers from the leading edge toward the perinuclear region is initiated. The final separation of the daughter cells then produces two polarized, migrating cells (Figure 13, cell separation). The cortical flow/solation–contraction coupling mechanism can explain significant aspects of the dynamics of both cytokinesis and polarized cell migration (Taylor and Fechheimer, 1982; Janson and Taylor, 1993; Kolega and Taylor, 1993; Giuliano and Taylor, 1994; Post *et al.*, 1995). The spatial domains of the cortical flow or transport of the actin and myosin II are modulated, in part, by the pattern of attachment to the substrate.

Investigating the Chemical and Molecular Dynamics of Cells

The technique of combining fluorescence-based reagents and light microscope-based imaging tools to define the chemical and molecular dynamics of living cells has reached a reasonable level of sophistication. Today there are a variety of commercially available reagents, automated microscopes, light detection systems, and powerful software packages (Taylor and Wang, 1989; Wang and Taylor, 1989; Mason, 1993). The multimode light microscope is one important stage in the evolution of the imaging technology. Future advances will come from linking high-performance computing with high-precision microscopes for real-time acquisition, processing, analysis, and display. These advances will permit the investigator to interact with the biological process as it occurs (Taylor *et al.*, 1996). In parallel, the first use of molecular biology to create fluorescence-based analogues and biosensors has accelerated the development of the next generation of reagents (Chalfie *et al.*, 1994; Giuliano *et al.*, 1995). These powerful in vivo tools, when coupled to the use of genetics and molecular genetics, will permit the definition of basic cell mechanisms.

Multimode light microscopy has enabled the cross-correlation of the structural and molecular dynamics of myosin II during cytokinesis in live cells. Given the apparent complexity of the temporal–spatial interplay of cellular components during cell division, it may be difficult to critically interpret experiments that involve the use of modulating reagents such as drugs, overexpressed proteins, and injected factors applied uniformly to cells. Thus, local activation of modulating reagents, through caging chemistry, is the method of choice to test correlations of temporal–spatial chemical and molecular events (Giuliano and Taylor, 1995). We are currently developing caged compounds for regulating phosphorylation spatially, as well as temporally, in an effort to dissect the intricate regulation of events resulting in cell division. The present results also demonstrate the importance of developing a phosphorylation biosensor for the inhibitory sites of the RLC of myosin II.

ACKNOWLEDGMENTS

We thank Kirk Cotter for image processing and technical assistance, Judy Montibeller for fluorescent probe preparation, and Charlotte

Bartosh for cell-culturing techniques. We appreciate the valuable suggestions provided by Drs. Kevin Burton, Ken Giuliano, Richard Fluck, and Charles Ettensohn. We thank Dr. Fred Lanni for his expertise in RIM data analysis and David Pane and Dr. Lowell Harris for their roles in developing the MPROC computer programs used in this study. This work was supported by the National Institutes of Health grant AR-32461, the National Science Foundation Science and Technology Center grant MCB-8920118, and the National Science Foundation High Performance Computing and Communications grant BIR-9217091.

REFERENCES

Agard, D.A. (1984). Optical sectioning microscopy: cellular architecture in three dimensions. Annu. Rev. Biophys. Bioeng. *13*, 191–219.

Amato, P.A., Unanue, E.R., and Taylor, D.L. (1983). Distribution of actin in spreading macrophages: a comparative study on living and fixed cells. J. Cell Biol. *96*, 750–761.

Bereiter-Hahn, J., Fox, C.H., and Thorell, B. (1979). Quantitative reflection contrast microscopy of living cells. J. Cell Biol. *82*, 767–779.

Bray, D., and White, J.G. (1988). Cortical flow in animal cells. Science *239*, 883–888.

Breckler, J., and Burnside, B. (1994). Myosin I localizes to the midbody region during mammalian cytokinesis. Cell Motil. Cytoskeleton *29*, 312–320.

Bright, G.R., Fisher, G.W., Rogowska, J., and Taylor, D.L. (1987). Fluorescence ratio imaging microscopy: temporal and spatial measurements of cytoplasmic pH. J. Cell Biol. *104*, 1019–1033.

Bright, G.R., and Taylor, D.L. (1986). Imaging at low light level in fluorescence microscopy. In: Applications of Fluorescence in the Biomedical Sciences, ed. D.L. Taylor, A.S. Waggoner, R.F. Murphy, F. Lanni, and R.R. Birge, New York: Alan R. Liss, 257–288.

Cao, L.G., and Wang, Y.L. (1990a). Mechanism of the formation of contractile ring in dividing cultured animal cells. I. Recruitment of pre-existing actin filaments into the cleavage furrow. J. Cell Biol. *110*, 1089–1095.

Cao, L.G., and Wang, Y.L. (1990b). Mechanism of the formation of contractile ring in dividing cultured animal cells. II. Cortical movement of microinjected actin filaments. J. Cell Biol. *111*, 1905–1911.

Chalfie, M., Tu, Y., Eusikirchen, G., Ward, W.W., and Prascher, D.C. (1994). Green fluorescent protein as a marker for gene expression. Science *263*, 802–805.

Chang, D.C., and Meng, C. (1995). A localized elevation of cytosolic free calcium is associated with cytokinesis in the zebrafish embryo. J. Cell Biol. *131*, 1539–1545.

Ciapa, B., Pesando, D., Wilding, M., and Whitaker, M. (1994). Cell-cycle calcium transients driven by cyclic changes in inositol triphosphate levels. Nature *368*, 875–878.

Condeelis, J., and Taylor, D.L. (1977). The contractile basis of amoeboid movement. V. The control of gelation, solation, and contraction in extracts from *D. discoideum*. J. Cell Biol. *74*, 901–927.

Conrad, P., Giuliano, K., Fisher, G., Collins, K., Matsudaira, P., and Taylor, D.L. (1993). Relative distribution of actin, myosin I, and myosin II during the wound healing response of fibroblasts. J. Cell Biol. *120*, 1381–1391.

Cramer, L.P., and Mitchison, T.J. (1995). Myosin is involved in postmitotic cell spreading. J. Cell Biol. *131*, 179–189.

Dan, K. (1954). The cortical movement in *Arbacia punctulata* eggs through cleavage cycles. Embryologia *2*, 115–122.

DeBiasio, R.L., Bright, G.R., Ernst, L.A., Waggoner, A.S., and Taylor, D.L. (1987). Five-parameter fluorescence imaging: wound healing of living Swiss 3T3 cells. J. Cell Biol. *105*, 1613–1622.

DeBiasio, R.L., Wang, L.L., Fisher, G.W., and Taylor, D.L. (1988). The dynamic distribution of fluorescent analogs of actin and myosin in protrusions at the leading edge of migrating Swiss 3T3 fibroblasts. J. Cell Biol. *107*, 2631–2645.

DeLozanne, A., and Spudich, J.A. (1987). Disruption of *Dictyostelium* myosin heavy chain gene by homologous recombination. Science *236*, 1086–1091.

Farkas, D.L., Baxter, G., DeBiasio, R.L., Gough, A., Nederlof, M.A., Pane, D., Pane, J., Patek, D.R., Ryan, K.W., and Taylor, D.L. (1993). Multimode light microscopy and the dynamics of molecules, cells, and tissues. Annu. Rev. Physiol. *55*, 785–817.

Fishkind, D.J., Cao, L.G., and Wang, Y.L. (1991). Microinjection of the catalytic fragment of myosin light chain kinase into dividing cells: effects on mitosis and cytokinesis. J. Cell Biol. *114*, 967–975.

Fishkind, D.J., and Wang, Y.L. (1993). Orientation and three-dimensional organization of actin filaments in dividing cultured cells. J. Cell Biol. *123*, 837–848.

Fishkind, D.J., and Wang, Y.L. (1995). New horizons for cytokinesis. Curr. Opin. Cell Biol. *7*, 23–31.

Fluck, R.A., Miller, A.L., and Jaffe, L.F. (1991). Slow calcium waves accompany cytokinesis in *medaka* fish eggs. J. Cell Biol. *115*, 1259–1265.

Fujiwara, K., and Pollard, T.D. (1976). Fluorescent antibody localization of myosin in the cytoplasm, cleavage furrow, and mitotic spindle of human cells. J. Cell Biol. *71*, 848–875.

Fukui, Y. (1993). Toward a new concept of cell motility: cytoskeletal dynamics in amoeboid movement and cell division. Int. Rev. Cytol. *144*, 85–127.

Fukui, Y., and Inoue, S. (1991). Cell division in *Dictyostelium* with special emphasis on actomyosin organization in cytokinesis. Cell Motil. Cytoskeleton *18*, 41–54.

Giuliano, K.A., Nederlof, M.A., DeBiasio, R., Lanni, F., Waggoner, A.S., and Taylor, D.L. (1990). Multimode light microscopy. In: Optical Microscopy for Biology, ed. B. Herman and K. Jacobson, New York: Wiley-Liss, 543–557.

Giuliano, K.A., Post, P., Hahn, K., and Taylor, D.L. (1995). Fluorescent protein biosensors. Annu. Rev. Biophys. Biomol. Struct. *24*, 405–434.

Giuliano, K.A., and Taylor, D.L. (1990). Formation, transport, contraction, and disassembly of stress fibers in fibroblasts. Cell Motil. Cytoskeleton *16*, 14–21.

Giuliano, K.A., and Taylor, D.L. (1994). Fluorescent actin analogs with a high affinity for profilin in vitro exhibit an enhanced gradient of assembly in living cells. J. Cell Biol. *124*, 971–983.

Giuliano, K.A., and Taylor, D.L. (1995). Measurement and manipulation of cytoskeletal dynamics in living cells. Curr. Opin. Cell Biol. *7*, 4–12.

Hahn, K., DeBiasio, R.L., and Taylor, D. (1992). Patterns of elevated free calcium and calmodulin activation in living cells. Nature *359*, 736–738.

Hahn, K., Kolega, J., Montibeller, J., DeBiasio, R.L., Post, P.L., Meyers, J., and Taylor, D.L. (1993). Fluorescent analogues: optical biosensors of the chemical and molecular dynamics of macromolecules in living cells. In: Fluorescent and Luminescent Probes for Biological Activity, ed. W.T. Mason, New York: Academic Press, 349–359.

Hepler, P.K. (1994). The role of calcium in cell division. Cell Calcium *16*, 322–330.

Hiramoto, Y. (1990). Mechanical properties of the cortex before and during cleavage. Cytokinesis. Ann. NY Acad. Sci. *582*, 22–29.

Hird, S.N., and White, J.G. (1993). Cortical and cytoplasmic flow polarity in early embryonic cells of *C. elegans*. J. Cell Biol. *121*, 1343–1355.

Hong, Y., Ernst, L., Wagner, M., and Waggoner, A. (1992). Sensitive detection of RNAs in single cells by flow cytometry. Nucleic Acids Res. *20*, 83–88.

Janson, L.W., Kolega, J., and Taylor, D.L. (1991). Modulation of contraction by gelation/solation in a reconstituted motile model. J. Cell Biol. *114*, 1005–1015.

Janson, L.W., and Taylor, D.L. (1993). In vitro models of tail contraction and cytoplasmic streaming in amoeboid cells. J. Cell Biol. *123*, 345–356.

Kiehart, D.P., Mabuchi, I., and Inoue, S. (1982). Evidence that myosin does not contribute to force production in chromosome movement. J. Cell Biol. *94*, 165–178.

Kitanishi-Yumura, T., and Fukui, Y. (1989). Actomyosin organization during cytokinesis: reversible translocation and differential redistribution in *Dictyostelium*. Cell Motil. Cytoskeleton *12*, 78–89.

Knecht, D.A., and Loomis, W.F. (1987). Antisense RNA inactivation of myosin heavy chain gene expression in *Dictyostelium discoideum*. Science *236*, 1081–1086.

Kolega, J., Janson, L.W., and Taylor, D.L. (1991). The role of solation–contraction coupling in regulating stress fiber dynamics in nonmuscle cells. J. Cell Biol. *114*, 993–1003.

Kolega, J., and Taylor, D.L. (1993). Gradients in the concentration and assembly of myosin II in living fibroblasts during locomotion and fiber transport. Mol. Biol. Cell *4*, 819–836.

Koppel, D.E., Oliver J.M., and Berlin, R.D. (1982). Surface functions during mitosis. III. Quantitative analysis of ligand-receptor movement into the cleavage furrow: diffusion vs. flow. J. Cell Biol. *93*, 950–960.

Lamb, N.J.C., Fernandez, A., Watrin, A., Labbe, J.C., and Cavadore, J.C. (1990). Microinjection of $p34^{cdc2}$ kinase induces marked changes in cell shape, cytoskeletal organization, and chromatin structure in mammalian fibroblasts. Cell *60*, 151–165.

Mabuchi, I. (1994). Cleavage furrow: timing of emergence of contractile ring actin filaments and establishment of the contractile ring by filament bundling in sea urchin eggs. J. Cell Sci. *107*, 1853–1862.

Mabuchi, I., and Itoh, T.J. (1992). Molecular mechanisms of mitosis and cytokinesis. In: Advances in Comparative and Environmental Physiology, ed. H. Sugi, Berlin, Germany: Springer-Verlag, 227–260.

Mabuchi, I., and Okuno, M. (1977). The effect of myosin antibody on the division of starfish blastomeres. J. Cell Biol. *74*, 251–263.

Mason, W.T. (1993). Fluorescent and Luminescent Probes for Biological Activity, New York: Academic Press.

Maupin, P., and Pollard, T.D. (1986). Arrangement of actin filaments and myosin-like filaments in the contractile ring and of actin-like filaments in the mitotic spindle of dividing HeLa cells. J. Ultrastruct. Mol. Struct. Res. *94*, 92–103.

Maupin, P., Phillips, C.L., Adelstein, R., and Pollard, T.D. (1994). Differential localization of myosin II isozymes in human cultured cells and blood cells. J. Cell Sci. *107*, 3077–3090.

Miller, K.G., and Kiehart, D.P. (1995). Fly division. J. Cell Biol. *131*, 1–5.

Mittal, B., Sanger, J.M., and Sanger, J.W. (1987). Visualization of myosin in living cells. J. Cell Biol. *105*, 1753–1760.

Post, P.L., DeBiasio, R.L., and Taylor, D.L. (1995). A fluorescent protein biosensor of myosin II regulatory light chain phosphorylation reports a gradient of phosphorylated myosin II in migrating cells. Mol. Biol. Cell *6*, 1755–1768.

Post, P.L., Trybus, K.M., and Taylor, D.L. (1994). A genetically engineered, protein-based optical biosensor of myosin II regulatory light chain phosphorylation. J. Biol. Chem. *269*, 12880–12887.

Rappaport, R. (1971). Cytokinesis in animal cells. Int. Rev. Cytol. *31*, 169–213.

Rappaport, R. (1986). Establishment of the mechanism of cytokinesis in animal cells. Int. Rev. Cytol. *105*, 245–281.

Salmon, E.D. (1989). Cytokinesis in animal cells. Curr. Opin. Cell Biol. *1*, 541–547.

Sanders, S.L., and Field, C.M. (1994). Septins in common? Curr. Biol. *4*, 907–910.

Sanger, J.M., Dome, J.S., Hock, R.S., Mittal, B., and Sanger, J.W. (1994). Occurrence of fibers and their association with talin in the cleavage furrows of PtK2 cells. Cell Motil. Cytoskeleton *27*, 26–40.

Sanger, J.M., Mittal, B., Dome, J.S., and Sanger, J.W. (1989). Analysis of cell division fusing fluorescently labeled actin and myosin in living PtK2 cells. Cell Motil. Cytoskeleton *14*, 201–219.

Sanger, J.W. (1975). Changing patterns of actin localization during cell division. Proc. Natl. Acad. Sci. USA *72*, 1913–1916.

Satterwhite, L.L., and Pollard, T.D. (1992). Cytokinesis. Curr. Opin. Cell Biol. *4*, 43–52.

Schroeder, T.D. (1990). The contractile ring and furrowing in dividing cells. Cytokinesis. Ann. NY Acad. Sci. *582*, 78–87.

Sellers, J.R., Pato, M.D., and Adelstein, R.S. (1981). Reversible phosphorylation of smooth muscle myosin, heavy meromyosin, and platelet myosin. J. Biol. Chem. *256*, 13137–13142.

Swann, M.M., and Mitchison, J.M. (1958). The mechanism of cleavage in animal cells. Biol. Rev. Camb. Philos. Soc. *33*, 103–135.

Tanasugarn, L., McNeil, P., Reynolds, G., and Taylor, D.L. (1984). Microspectrofluorimetry by digital image processing: measurement of cytoplasmic pH. J. Cell Biol. *98*, 717–724.

Taylor, D.L., Condeelis, J.S., Moore, P.L., and Allen, R.D. (1973). The contractile basis of amoeboid movement. I. The chemical control of motility in isolated cytoplasm. J. Cell Biol. *59*, 378–394.

Taylor, D.L., and Fechheimer, M. (1982). Cytoplasmic structure and contractility: the solation–contraction coupling hypothesis. Philos. Trans. R. Soc. Lond. B. Biol. Sci. *299*, 185–197.

Taylor, D.L., Harris, L.D., DeBiasio, R., Fahlman, S.E., Farkas, D.L., Lanni, F., Nederlof, M., and Gough, A.H. (1996). Automated interactive microscopy: measuring and manipulating the chemical and molecular dynamics of cells and tissues. Proc. SPIE *2678*, (*in press*).

Taylor, D.L., Nederlof, M.A., Lanni, F., and Waggoner, A.S. (1992). The new vision of light microscpy. Am. Sci. *80*, 322–335.

Taylor, D.L., and Salmon, E.D. (1989). Basic fluorescence microscopy, part A In: Methods in Cell Biology, vol 29, New York: Academic Press.

Taylor, D.L., and Wang, Y.L. (1978). Molecular cytochemistry: incorporation of fluorescently labeled actin into living cells. Proc. Natl. Acad. Sci. USA *75*, 857–861.

Taylor, D.L., and Wang, Y.L. (1980). Fluorescently labelled molecules as probes of the structure and function of living cells. Nature *284*, 405–410.

Taylor, D.L., and Wang, Y.L. (1989). Fluorescence microscopy of living cells in culture, part B. In: Methods in Cell Biology, vol 29, New York: Academic Press.

Verkhovsky, A.B., and Borisy, G.G. (1993). Nonsarcomeric mode of myosin II organization in the fibroblast lamellum. J. Cell Biol. *123*, 637–652.

Wang, Y.L. (1985). Exchange of actin subunits at the leading edge of living fibroblasts: possible role of treadmilling. J. Cell Biol. *101*, 597–602.

Wang, Y.L., Silverman, J.D., and Cao, L.G. (1994). Single particle tracking of surface receptor movement during cell division. J. Cell Biol. *127*, 963–971.

Wang, Y.L., and Taylor, D.L. (1979). Distribution of fluorescently labeled actin in living sea urchin eggs during early development. J. Cell Biol. *82*, 672–679.

Wang, Y.L., and Taylor, D.L. (1989). Fluorescence microscopy of living cells in culture, part A. In: Methods in Cell Biology, vol 29, New York: Academic Press.

White, J.G., and Borisy, G.G. (1983). On the mechanism of cytokinesis in animal cells. J. Theor. Biol. *101*, 289–316.

Wolpert, L. (1960). The mechanics and mechanism of cleavage. Int. Rev. Cytol. *10*, 163–216.

Yamakita, Y., Yamashiro, S., and Matsumura, F. (1994). In vivo phosphorylation of regulatory light chain of myosin II during mitosis of cultured cells. J. Cell Biol. *124*, 129–137.